Ocean Engineering 285 (2023) 115332

Contents lists available at ScienceDirect

Ocean Engineering

journal homepage: www.elsevier.com/locate/oceaneng

A holistic optimization tool for the design of power take-off systems in realistic wave climates: The Wells turbine case

Ander Zarketa-Astigarraga [a,*], Alain Martin-Mayor [a], Aimar Maeso [b], Borja de Miguel [b], Manex Martinez-Agirre [a], Markel Penalba [a,c]

[a] Mondragon Unibertsitatea, Faculty of Engineering, Mechanical and Industrial Production, Loramendi 4, Mondragon, 20500 Gipuzkoa, Spain
[b] IDOM Consulting, Engineering, Architecture S.A.U., Bilbao, Spain
[c] Ikerbasque, Basque Foundation for Science, Euskadi Plaza 5, 48011 Bilbao, Spain

ARTICLE INFO

Keywords:
Wells turbines
Genetic algorithm
Blade optimization
BEM analysis

ABSTRACT

The growing demand of energy coupled with the worldwide commitments in favor of renewable technologies turns marine renewable sources especially attractive, including wave energy. In particular, the oscillating water column technology is shown to be one of the most promising technologies, for which the design of efficient air turbines is crucial. The large number of geometrical parameters that such turbines own, together with the fact that the wave climate conditions affect the overall behavior, call for a tool that combines both aspects for optimizing the turbine design. A genetic-algorithm-based approach is proposed, which runs over a blade-element-method coupled with a stochastic modeling of the sea-state. The optimization method computes an overall fitness function given as a weighted average of the stochastic turbine efficiency over a set of most relevant sea-states. The suggested methodology is proven capable of finding the global fitness maximum upon a 6-dimensional parametric space. Additionally, it allows identifying and discarding the geometrical parameters that are shown to be negligible for the computation of the fitness function. Hence, a reduced parametric space results in a 2-dimensional region comprised by the hub-to-tip ratio and the tip solidity, which permits refining the search and analyzing their individual effects upon the turbine design. It is shown that the optimal configuration corresponds to trade-off solutions between the hub-to-tip ratio and the tip solidity, avoiding both an excessive rotational speed and an exceeding blockage of the turbine.

1. Introduction

The concerns about climate change, as well as the need to mitigate its effects in a near future, have led to international cooperation attempts seeking for viable solutions, with treatises such as the Paris Agreement advocating for the so-called net zero commitments (United Nations, 2022b). These commitments urge the subscriber countries to reduce the emissions by 45% by 2030, and to set them as close to zero as possible by 2050 (United Nations, 2022a). Among the master guidelines for achieving such goals, replacing carbon-based energy sources with renewable ones constitutes a primary milestone. Within the set of currently available technologies, offshore renewable energy still stands as a largely untapped resource, although its potential to promote the decarbonization of the energy system is significant (Addamo et al., 2022; Li et al., 2022; Hu et al., 2022). Among offshore renewable energy technologies, offshore wind, including floating technologies, has already reached the commercial level, while tidal and wave energy are still a step behind. Despite its relatively lower level of maturity, wave energy can significantly contribute to the energy transition, particularly due to the capacity to provide a more consistent energy flow that is highly compatible with other sources (Fusco et al., 2010).

1.1. Wave energy: OWCs and Wells turbines

Within the variety of wave converter prototypes, oscillating water column (OWC) devices are considered as one of the most promising technologies (Falcão, 2010; Falcão and Henriques, 2016; Alves et al., 2021; Ciappi et al., 2022; Gato et al., 2022). The notion of an OWC addresses an either fixed or floating chamber that is semi-submerged in the water, with one of its ends open to the sea and the other to the atmosphere, as illustrated in Fig. 1. The chamber is designed so that the waves entering from the sea-side end conform a free-surface, setting the air above it in motion. The oscillating motion of the water column alternately compresses and decompresses the air, whose kinetic energy can be harvested by placing a turbine close to the atmospheric end of the chamber. Given the bidirectional nature of the air flow, the turbine

* Corresponding author.
E-mail address: azarketa@mondragon.edu (A. Zarketa-Astigarraga).

https://doi.org/10.1016/j.oceaneng.2023.115332
Received 27 February 2023; Received in revised form 4 July 2023; Accepted 6 July 2023
Available online 20 July 2023

Nomenclature

Acronyms

BEM	Blade element method
CFD	Computational fluid dynamics
GA	Genetic algorithm
OWC	Oscillating water column
WEC	Wave energy converter

Superscripts

$\bullet'$	Referential value
$\bar{\bullet}$	Stochastically-averaged value

Subscripts

Δp	Pressure-drop-related value
$\frac{N}{2}$	Value at midspan
Φ	Flow-coefficient-related value
Π	Dimensionless-power-related value
Ψ	Dimensionless-pressure-drop-related value
θ	Tangential component
a	Atmospheric value
d	Drag-related value
i	Generic blade element index
j	Generic iteration index
$j-1$	Previous iteration index
l	Lift-related value
P	Power-related value
Q	Flow-rate-related value
r	Radial component
tc	Induced-drag-related value
x	Axial component
1	Value at turbine inlet
2	Value at turbine outlet
av.	Averaged value
CIF	Interference-factor-corrected value
fit	Fitted value
hub	Value at hub
min	Maximum value
min	Minimum value
SS	Sea-state-related value
tip	Value at tip

Variables

α	Absolute velocity angle
β	Relative velocity angle
δf	Differential load
Δp	Pressure drop across turbine
η	Efficiency of the turbine
$\mathcal{N}$	Number of sea-states
t	Tip clearance
μ	Air viscosity
ν	Hub-to-tip ratio
ω	Rotational speed
Φ	Dimensionless flow-parameter of the turbine
Π	Dimensionless power delivered by the turbine
Ψ	Dimensionless pressure drop across the turbine
ρ	Air density
σ	Solidity standard deviation
τ	Torque developed by the turbine
ε	Error tolerance
c	Chord
C_p	Damping coefficient
f	Fitness function probability density function
K	Slope of linear $\Psi-\Phi$ relation
N	Number of blade elements
P	Power delivered by the turbine
p	Air pressure
Q	Flow-rate
r	Radial coordinate
U	Tangential velocity
v	Absolute velocity
w	Relative velocity
Z	Blade number
Re	Reynolds number

must be capable of maintaining its rotational direction unchanged, which leads to the so-called self-rectifying turbine designs. The most common types among them are the Wells turbine (Wells, 1976) and the impulse turbine (Babintsev, 1975), reviews of which can be found in Setoguchi and Takao (2006), Falcão (2010), Falcão et al. (2014), Falcão and Henriques (2016) and Shehata et al. (2016).

The main reason for focusing on Wells turbines stems from their relative simplicity, both on the conceptual and mechanical aspects. The simplest version of a Wells turbine comprises a rotor with a set of blades shaped symmetrically and whose chordal plane is perpendicular to the rotational axis, thus ensuring the self-rectifying feature of the design (Wells, 1976). Parting from such an original conception, the modifications proposed for enhancing the efficiency of the turbine have been many. An early and detailed study by Raghunathan thoroughly introduces the notions of a biplane Wells turbine and the so-called guide vanes (Raghunathan, 1995); the former are conceived with the purpose of augmenting the power extracted by the turbine, whereas the latter have the aim of directing the flow and reducing the loss of kinetic energy due to the swirl component of the outflow (Raghunathan, 1995; Alves et al., 2021). The same study identifies relevant geometrical design parameters such as the turbine solidity, the hub-to-tip ratio, the aspect ratio, the tip clearance, and the radial distribution of airfoil profiles and thickness ratios (Raghunathan, 1995).

Ever since, experimental tests upon different turbine configurations have revealed important behavioral aspects of Wells turbines. Studies upon configurations with different solidities have shown that larger values of the parameter induce a higher swirl component downstream the rotor and a lower efficiency overall, a handicap that is partly mitigated by the use of guide vanes, especially in biplane turbines (Curran and Gato, 1997; Falcão et al., 2018; Alves et al., 2021). The studies also show that the increase in efficiency experienced by the turbines depends on the particular configuration of guide vanes employed, being different to use a single row placed between the rotor stages of a biplane, or a double set of symmetrical vanes located upstream and downstream the turbine. Overall, the guide vanes are shown to enhance the efficiency of a monoplane rotor from 0.52 to 0.71 (Curran and Gato, 1997; Falcão et al., 2018), and that of a biplane from 0.55 to 0.62 (Alves et al., 2021). The use of end plates that modify the gap between the tip and the casing have been shown to increase the efficiency due to the reduction of tipward three-dimensional effects (Takao et al., 2007; Shehata et al., 2016). The spanwise distributions of blade skew, pitch angle and chordal dimensions are also shown to affect

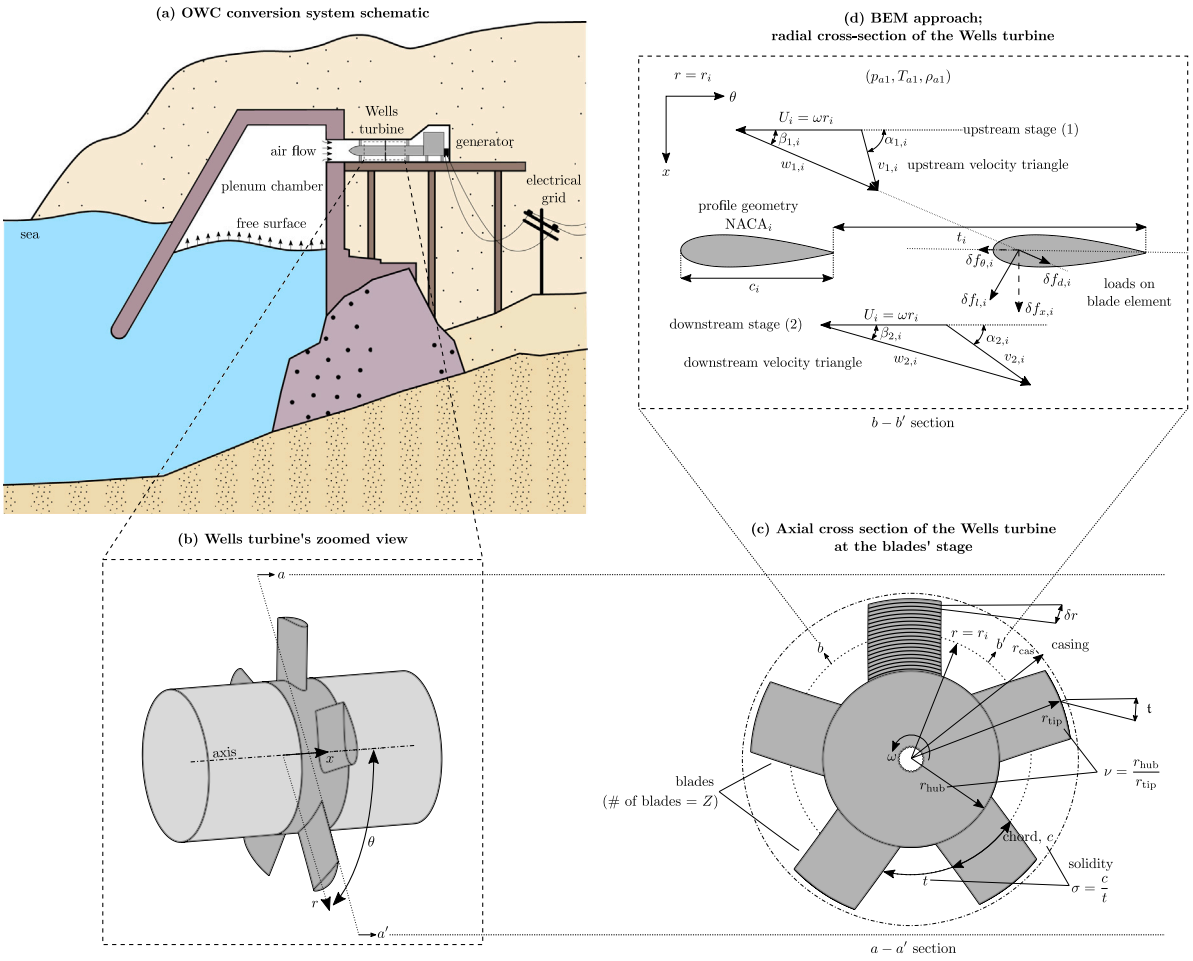

Fig. 1. (a): schematic of an OWC system; (b) definition of cylindrical coordinates upon Wells turbine; (c) main geometrical parameters of a Wells turbine; (d) linear cascade approach of a Wells turbine for BEM application.

the behavior of the turbine (Setoguchi et al., 1997; Gato and Webster, 2001; Kinoue et al., 2002; Starzmann and Carolus, 2011, 2013, 2014; Shehata et al., 2016). Swept blades are reported to induce an efficiency enhancement within a wider range of operation conditions, to the cost of a loss in peak efficiency (Gato and Webster, 2001). Additionally, such a skew is shown to reduce acoustic noise by up to 4 dB as compared to the unswept baseline turbine blades, together with an increase in efficiency that comes from extending the range of stall-free operation by 106% (Starzmann and Carolus, 2013). Pitching the blades is observed to provide better starting characteristics and lower operation speed requirements than baseline configurations, as well as reducing the aerodynamic losses and enhancing the overall efficiency (Setoguchi et al., 1997). Additionally, studies performed with a set of turbines showing different distributions of spanwise chordal and airfoil profile distributions, as well as differing hub-to-tip ratios, show that the optimum choice of geometrical parameters can vary noticeably depending on the outcome to be maximized (Starzmann and Carolus, 2011, 2014). Thus, moderate values of solidity and hub-to-tip ratio are recommended if the aim is to achieve large efficiencies or to control the slope of the pressure-flow curve (Starzmann and Carolus, 2013); instead, low values of both parameters are preferred for extending the stall-free operation regime, thus avoiding the acoustic noise induced by stalled blades (Starzmann and Carolus, 2011, 2013).

Numerical studies on Wells turbines also abound (Dhanasekaran and Govardhan, 2005; Torresi et al., 2008, 2009; Mohamed and Shaaban, 2013; Kumar et al., 2019; Abbasi and Ketabdari, 2022; Kotb et al., 2022). Some of the works addressed before, in fact, combine both approaches (Starzmann and Carolus, 2013; Ciappi et al., 2020, 2022). The earliest CFD attempts tried to reproduce experimental results by Reynolds-Averaged Navier–Stokes (RANS) based simulations employing the $k - \varepsilon$ model, both on pre- and post-stall conditions, and showed an acceptable match between both data-sets (Dhanasekaran and Govardhan, 2005). Further studies have dealt with a comparative analysis among RANS turbulence models, namely the Spalart–Allmaras, $k - \omega$ and Reynolds-stress formulations, and their predictive power for determining the effect of tip-leakage and turbine solidity on the overall performance (Torresi et al., 2008, 2009), or showing the relatively poorer behavior of CFD simulations when reproducing near-stall conditions (Starzmann and Carolus, 2013). More advanced studies have introduced the pitch variability in the simulations, showing an increase of 2.3% in turbine efficiency and matching the trends observed experimentally (Mohamed and Shaaban, 2013). Recent studies have already approached the problem from a geometrical standpoint, introducing modifications upon the turbine design, such as radiused edge tips, extended trailing edges, variable blade thicknesses, Gurney flaps or sharkskin-based riblets (Kumar et al., 2019; Abbasi and Ketabdari, 2022; Kotb et al., 2022). It is claimed that a combination of some of the modifications can improve the stall margin and turbine power by 22% and 97% respectively, although at the cost of decreasing the relative efficiency by 7.7% (Kumar et al., 2019). The same qualitative results are obtained with the Gurney flap, achieving an increment in torque coefficient of 81.11%, though a smaller stall delay coupled with an efficiency drop (Kotb et al., 2022). In the case of the riblets, the drag reduction they induce leads to an average efficiency enhancement of 2.33% (Abbasi and Ketabdari, 2022).

1.2. An industry-oriented optimization framework

The significant bibliographical corpus on Wells turbines reveals that, despite the well-founded understanding of the individual parameters that affect the overall behavior of the turbine, the inter-dependencies among these geometrical parameters and, especially, the effect of the hydrodynamic and pneumatic performance of the device are not adequately understood. This sets forth a potential optimization problem whose aim is to determine the values of such parameters that maximize a given metric of the turbine's behavior as a function of the specific device the turbine is implemented in, and the geographical location the device is deployed.

Optimization strategies are not new to the fields of aerodynamics and turbomachinery, with several approaches having been applied in recent studies for finding the optimal shapes of blades in small- (Arumugam et al., 2021) and large-scale wind-turbines (Ji et al., 2021), impellers (Pourrajabian et al., 2021), tidal devices (Yeo et al., 2022) and, more relevantly, Wells turbines (Gato and Henriques, 1996; Mohamed et al., 2011; Ghisu et al., 2011; Mohamed and Shaaban, 2013; Shaaban, 2017; Halder et al., 2018; Gratton et al., 2018; Mahrooghi and Lakzian, 2021; Ciappi et al., 2022; Das et al., 2022). A thorough review of the optimization strategies employed in the field of Wells turbines shows that, although techniques as diverse as gradient-based, surrogate-based or tabu search exist, evolutionary programming approaches of the genetic algorithm (GA) sort are the most widely used ones (Das et al., 2022).

Besides the strategy itself, the literature shows two relevant aspects that determine the optimization approach are the fitness function being maximized and the set of variables constituting the parametric set to be optimized. With respect to the first aspect, the addressed bibliography shows that the choices do not abound: there are studies that consider the maximization of the torque coefficient or the tangential force (Gratton et al., 2018), others that include, additionally, the maximization of efficiency (Mohamed et al., 2011; Mohamed and Shaaban, 2013; Halder and Samad, 2016; Shaaban, 2017; Halder et al., 2018; Mahrooghi and Lakzian, 2021), and works that attempt at minimizing the adverse pressure gradient along the blades (Gato and Henriques, 1996). As may be noticed, all the employed fitness functions focus on enhancing the aerodynamic behavior of the turbine configurations.

With respect to the geometrical parameters to be optimized, the mentioned studies propose a relatively low-dimensional set of design variables aimed at modifying the shape of the blades. Thus, the optimization is applied upon the pitch angle (Mohamed and Shaaban, 2013), the control points upon the profile (Mohamed et al., 2011; Gratton et al., 2018), thickness-related parameters (Shaaban, 2017; Halder and Samad, 2016; Halder et al., 2018; Gato and Henriques, 1996) or the sweep angle (Halder and Samad, 2016; Halder et al., 2018). The absence of certain essential variables of Wells turbines such as the hub-to-tip ratio, the tip clearance or the hub and tip solidities may stem from the fact that their effects on the aerodynamic behavior have been properly established in thorough studies, as mentioned before (Raghunathan, 1995).

However, the main caveat of the optimizations cited above may come from the fact that they restrict the analytical focus to the aerodynamic part of the OWC device. It is known, though, that an OWC plant is highly sensitive to the wave climate conditions that affect the sea state determining the behavior of the turbine, and that such conditions may be modeled as stochastic processes (Falcão and Rodrigues, 2002). As shown recently, such an stochastic feature of the sea state has a critical effect on the energetic outcome of the Wells turbines (Falcão et al., 2018; Alves et al., 2021). As a consequence, ideally, the hydrodynamics and pneumatic performance of the wave energy converter (WEC), including the control action, should also be taken into account when launching an optimization campaign.

Thus, the coupling between the hydrodynamics and pneumatic effects of WECs, and the aerodynamics of Wells turbines sets forth a new optimization scenario. There are two main features that determine such a scenario: first, it requires stepping back on the detailed knowledge about the individual effects induced by the geometrical parameters, as explained in Raghunathan (1995). It is sensible to assume that the inclusion of the WEC induce unknown inter-dependencies among the geometrical variables. Accordingly, the parametric space of the optimization problem needs to be properly extended with respect to the aforementioned studies, including variables such as the number of blades, the hub-to-tip ratio or the solidities, in addition to the shape of the blades. Second, and more relevant, is the choice of the fitness function to be maximized, as it shall constitute a combined metric representing the holistic behavior of the WEC.

A proposal for such a metric is provided in the current study, and it is conceived as a weighted stochastic efficiency across a realistic wave climate that results from the turbine being subjected to a set of most energetic sea states. Dependent as it is to the characteristics of a specific WEC and realistic wave climate conditions, the optimization case-study analyzed herein is run upon a real OWC device. On this respect, the proposed optimization shows the additional value of being a realistic, industry-oriented case-study.

Finally, the industry-oriented philosophy asks for a solving procedure that complies with both the temporal and material resources of industrial engineering workflows. As the optimization strategy aims at identifying potential turbine configurations at the initial design stage, with their fine-tuning taking place at further steps, it is sensible to devise a tool that allows fast and efficient calculations. An analytical model is proposed for such a purpose, which is considered as a side contribution in addition to the optimization strategy itself. The novelty comes from both the holistic hydro-aerodynamic approach, including the action of the controller, and the fact that a thorough mathematical derivation is provided, as aerodynamic analytical tools on Wells turbines as such abound in the literature (Raghunathan et al., 1982; Gato and Falcão, 1984; Gato and De, 1988, 1989; Ciappi et al., 2022; Licheri et al., 2022). Thus, the contributions of the current work may be summarized as (i) articulating a holistic hydro-aerodynamic optimization approach on the geometrical parameters of Wells turbines considering realistic wave climates and the impact of control action, (ii) analyzing a realistic, industry-oriented case-study, and (iii) providing an analytical-model-based fast tool for carrying out the calculations. Although the present study focuses on OWC devices and air turbines, the same optimization approach can be extended to any other type of WEC and power take-off technology.

Complying with such goals, the paper is structured so that Section 2 outlines the minimal theoretical notions of the stochastic approach used for modeling the sea-states. Section 3 provides the specifications of the case-study to analyzed, both from the standpoint of the geometrical parameters to be analyzed and from the sea-states conditions that the system may face. Section 4 shows the results of the study, and discusses the key aspects of them. Finally, Section 5 draws the most relevant conclusions and marks the possible future lines.

2. Theoretical framework

This section describes (i) the analytical model employed and its sanctioning in Section 2.1, and (ii) the stochastic model accounting for the variability of realistic wave climates in Section 2.2. The descriptions of the models are kept as minimal as possible, providing all the required information to reproduce the model and addressing the interested reader to the referential studies in case further details are required.

2.1. Analytical model of a Wells turbine

2.1.1. Coordinate frames and geometrical input parameters

Fig. 1 sets the layout of the system to be analyzed. Fig. 1(a) is a schematic view of an OWC-based conversion system, with a monoplane Wells turbine with no guide vanes being outlined in Fig. 1(b) and

constituting the case-study of the work. The cylindrical coordinate system comprises the (x, r, θ) triplet that correspond to the axial, radial and tangential directions, respectively.

The geometrical parameters that determine the Wells turbine are detailed in Fig. 1(c), which shows the axial plane of the rotor:

- Z: stands for the number of blades of the rotor.
- r_{hub}: is the hub radius of the turbine.
- r_{tip}: is the tip radius of the turbine.
- ν: represents the hub-to-tip ratio, namely $\nu = r_{\text{hub}}/r_{\text{tip}}$.
- r_{cas}: is the casing radius of the turbine.
- t: stands for the tip clearance or gap between the tip and casing of the turbine. It is usually given in relative percentage with respect to the chordal dimension at the tip.
- $c\,(r)$: it is the chordal dimension at each radial stage.
- $t\,(r)$: corresponds to the distance between blades, namely the one between leading- or trailing-edges.
- $\sigma\,(r)$: the solidity parameter, which corresponds to the ratio of the circumferential perimeter occupied by the blades at each radial stage, i.e. $\sigma\,(r) = c/t$.
- ω: it is the rotational velocity of the turbine. It is not a geometrical parameter itself, but it represents an input variable nonetheless.

2.1.2. BEM approach in a nutshell

The simplest model accounting for the aerodynamic behavior of a Wells turbine considers a steady, incompressible, irrotational, axisymmetric and radially-on-equilibrium flow (Raghunathan et al., 1982; Raghunathan, 1995), a set of assumptions under which the so-called blade element momentum (BEM) theory becomes applicable to the system (Ciappi et al., 2020, 2022).

The BEM approach allows for a two-dimensional analysis of the flow. The radial dimension of the turbine is split into a number of infinitesimally wide circumferences. The features of the simplified flow permit studying each of those slices separately, given that the restrictive conditions imposed on the flow ensure the independence of the dynamics taking place between adjacent slices. Thus, the problem may be reduced to the analysis of the rectilinear cascade depicted on Fig. 1(d). Such a cascade corresponds to a generic cross-sectional plane located at the radial distance $r = r_i$, with $i \in [1, N]$ being a dummy index addressing the particular infinitesimal circumference chosen for the analysis.

The upper and lower velocity triangles depicted on Fig. 1(d) correspond, respectively, to the upstream and downstream kinematic states of the flow, assuming that the air travels from top to bottom. The cross-sectional planes of the blades are reduced to their profiles, and they constitute the so-called blade elements. Due to the rotary motion of the turbine, both triangles own absolute (v) and a relative (w) velocity components. The upstream velocities are subscripted with the label (1), whereas the downstream ones are tagged with a (2). The tangential velocity $U_i = \omega r_i$ does not vary when crossing the rotor ($U_{1,i} = U_{2,i}$), but the tangential projections of either the absolute ($v_{\theta 1,i} \neq v_{\theta 2,i}$) or the relative velocity vectors do ($w_{\theta 1,i} \neq w_{\theta 2,i}$), which is the principle whereby turbomachinery devices operate according to the Euler equation (Scholz, 1977).

The BEM approach relates the changes in the velocity triangles to the aerodynamic loads experienced by the blade elements, i.e. the differential lift ($\delta f_{l,i}$) and drag ($\delta f_{d,i}$) loads depicted on Fig. 1(d) that act along the perpendicular and parallel directions with respect to w_1, respectively. Once the loads are obtained, it is possible to calculate the differential torques and pressure drops and, by integration, the energetic outcome of the Wells turbine.

2.1.3. Actuator-disk approach in a nutshell

A disadvantage of the BEM approach is that it does not account for radial variations of the axial velocity component, even if such variations are known to be relevant for determining the turbine's behavior (Hawthorne and Horlock, 1962; Scholz, 1977). The actuator-disk theory is the simplest one that allows introducing radial variations in the model, turning it into a semi-3D approach (Hawthorne and Horlock, 1962; Gato and Falcão, 1984; Gato and De, 1988, 1989).

The theory replaces the finite-dimensional rotor plane with an infinitely thin disk that induces a discrete jump on the energy-carrying variables such as the enthalpy or the pressure-drop. However, it makes the mass-flux and, consequently, the radial velocity component redistribute in the fore and aft regions of the rotor plane, at the time it ensures a continuous variation of them across the disk. This leads to a better agreement with experimental tests (Hawthorne and Horlock, 1962), and it constitutes an enhancement with respect to the BEM theory in which the whole of the radial velocity change is confined to the finite-dimensional rotor plane, turning the resultant flow unrealistic. Besides, implementing the actuator-disk approach in combination with the BEM theory requires, merely, the imposition of an energy conservation criterion as in Ciappi et al. (2020), Ciappi (2020) and Ciappi et al. (2022), adding a negligible extra computational burden.

2.1.4. Equations of the analytical model

For the sake of conciseness, the equations of the combined BEM/actuator-disk approach are reduced to the minimal ones required for computing the energetic outcome of a Wells turbine. The reader interested in following the mathematical reasoning in detail is referred to Ciappi (2020).

In addition to the assumptions made so far, the following are required to carry set the analytical framework properly:

- The incoming flow's absolute velocity and its direction, namely $v_{x1,i}$ and $\alpha_{1,i}$. The absolute velocity will be considered uniform and purely axial across the blade passage, i.e.:

$$\left.\begin{array}{ll} v_{x1,i} = v_1 & \text{(a)} \\ \alpha_{1,i} = \frac{\pi}{2} & \text{(b)} \end{array}\right\} \forall i \in [1, N] \tag{1}$$

  The triplet (ω, v_1, α_1) constitutes the set of operational parameters provided to the model.
- The pressure (p_a), density (ρ_a) and viscosity (μ_a) of the fluid are considered uniform across the passage. The triplet (p_a, ρ_a, μ_a) constitutes the set of flow parameters provided to the model.
- The geometry of the airfoils is represented as NACA$_i$ in Fig. 1(d), which means that the profiles considered in the present analysis are reduced to symmetric NACA shapes, according to the self-rectifying feature of the Wells design and that are the most employed airfoils according to the bibliography (Gato and Henriques, 1996; Mohamed et al., 2011; Mohamed and Shaaban, 2013; Halder and Samad, 2016; Gratton et al., 2018; Halder et al., 2018; Alves et al., 2021; Mahrooghi and Lakzian, 2021; Ciappi et al., 2022; Das et al., 2022; Licheri et al., 2022); the subscript i allows for the radial variation of the blade geometry. In nay case, extending the analysis to other blade profiles is straightforward.

The equations of the model are reduced to the (i) upstream kinematic relations; (ii) dynamic relations; (iii) downstream kinematic relations; (iv) radial equilibrium imposition; (v) integrated energetic relations; and (vi) actuator-disk implementation.

(i) Upstream kinematic relations: together with Eqs. (1)(a) and (1)(b), the expressions that determine the upstream velocity triangle are:

$$U_i = \omega r_i \,, \tag{2}$$

$$\left.\begin{array}{ll} v_{\theta 1,i} = 0 & \text{(a)} \\ w_{x1,i} = v_1 & \text{(b)} \end{array}\right\} \forall i \in [1, N] \tag{3}$$

$$w_{\theta 1,i} = -U_i \ , \tag{4}$$

$$w_{1,i} = \sqrt{w_{x1,i}^2 + w_{\theta 1,i}^2} \ , \tag{5}$$

$$\beta_{1,i} = \tan^{-1}\left(\frac{w_{x1,i}}{w_{\theta 1,i}}\right) \ , \tag{6}$$

$$\boldsymbol{\Phi}_{1,\frac{N}{2}} = \frac{v_{x1,\frac{N}{2}}}{U_{\frac{N}{2}}} = \boldsymbol{\Phi} \ . \tag{7}$$

The symbol $\boldsymbol{\Phi}$ in Eq. (7) denotes the dimensionless flow coefficient. Its upstream midspan value ($\boldsymbol{\Phi}_{1,\frac{N}{2}}$) is used for characterizing the input to the turbine.

(ii) Dynamic relations: the triplet $\left(\text{NACA}_i, \beta_{1,i}, \text{Re}_i\right)$ determines the lift ($C_{l,i}$) and drag ($C_{d,i}$) coefficients, which constitute the dimensionless counterparts of the respective loads. The panel-method-based XFoil code (Drela, 1989) is employed for obtaining the Reynolds- and angle-of-attack-based polars in a way complying with the fast feature of the analytical tool, as in Gato and Henriques (1996). The loads themselves are obtained by turning the corresponding coefficients dimensional. As for the drag load, the actual value is expressed as $\delta f_{d_{tc},i}$, where the tc subscript addresses the fact that the tip clearance, or the tipwards gap, causes an extra contribution to the force, which is computed by modifying the drag coefficient ($C_{d_{tc},i}$) accordingly.

$$\text{Re}_i = \frac{\rho_a w_{1,i} c_i}{\mu_a} \ , \tag{8}$$

$$\delta f_{l,i} = \frac{1}{2}\rho_a c_i w_{1,i}^2 C_{l,i}\left(\text{NACA}_i, \beta_{1,i}, \text{Re}_i\right)\delta r \ , \tag{9}$$

$$C_{d_{tc},i} = C_{d,i}\left(\text{NACA}_i, \beta_{1,i}, \text{Re}_i\right) + 0.7\frac{C_{l,i}\left(\text{NACA}_i, \beta_{1,i}, \text{Re}_i\right)\cdot t_i}{r_{\text{hub}}\left(\frac{1}{\nu}-1\right)} \ , \tag{10}$$

$$\delta f_{d_{tc},i} = \frac{1}{2}\rho_a c_i w_{1,i}^2 C_{d_{tc},i}\left(\text{NACA}_i, \beta_{1,i}, \text{Re}_i\right)\delta r \ . \tag{11}$$

The axial and tangential forces are obtained by projecting the lift and drag loads upon the corresponding axes. The interference between different blades is accounted for by a semi-empirical correction factor provided in Raghunathan (1995), which depends solely on σ_i and whose consideration is reflected on the CIF label of the subscripts.

$$\delta f_{x,i_{\text{CIF}}} = \frac{1}{1-\sigma_i^2}\left(\delta f_{l,i}\cos\beta_{1,i} + \delta f_{d_{tc},i}\sin\beta_{1,i}\right) \tag{12}$$

$$\delta f_{\theta,i_{\text{CIF}}} = \frac{1}{1-\sigma_i^2}\left(\delta f_{l,i}\sin\beta_{1,i} - \delta f_{d,i}\cos\beta_{1,i}\right) \tag{13}$$

(iii) Downstream kinematic relations: in the expressions below, $C_{\theta,i_{\text{CIF}}}$ is the dimensionless counterpart of the $\delta f_{\theta,i_{\text{CIF}}}$ load.

$$\alpha_{2,i} = \cot^{-1}\left(\cot\alpha_{1,i} + \frac{Z c_i C_{\theta,i_{\text{CIF}}}}{4\pi r_i \sin\beta_{1,i}^2}\right) \ , \tag{14}$$

$$v_{x2,i} = v_{x1,i} \ , \tag{15}$$

$$v_{\theta 2,i} = v_{x2,i}\cot\alpha_{2,i} \ , \tag{16}$$

$$v_{2,i} = \sqrt{v_{x2,i}^2 + v_{\theta 2,i}^2} \ , \tag{17}$$

$$w_{x2,i} = v_{x2,i} \ , \tag{18}$$

$$w_{\theta 2,i} = v_{\theta 2,i} - U_i \ , \tag{19}$$

$$w_{2,i} = \sqrt{w_{x2,i}^2 + w_{\theta 2,i}^2} \ , \tag{20}$$

$$\beta_{2,i} = \tan^{-1}\left(\frac{w_{x2,i}}{w_{\theta 2,i}}\right) \ . \tag{21}$$

(iv) Radial equilibrium imposition: derives from the constancy of the total pressure along the span (Raghunathan, 1995; Ciappi, 2020), which leads to the following expression:

$$\frac{\mathrm{d}\left(v_{x2,i}^2\right)}{\mathrm{d}r} = -\frac{1}{4\pi^2 r_i^2}\frac{\mathrm{d}\left(2\pi r_i v_{\theta 2,i}\right)^2}{\mathrm{d}r} \ . \tag{22}$$

Solving the differential equation above leads to a new distribution of downstream axial velocities, namely $v'_{x2}(r)$. The continuity condition is employed for checking whether the calculated distribution is valid; considering incompressible flow:

$$Q = \int_{r_{\text{hub}}}^{r_{\text{tip}}} 2\pi r v_{1x}(r)\,\mathrm{d}r = \int_{r_{\text{hub}}}^{r_{\text{tip}}} 2\pi r v_{2x}(r)\,\mathrm{d}r = Q' \ . \tag{23}$$

On practical grounds, Eq. (23) is checked by setting a tolerance ε_Q below which the difference between Q and Q' is assumed to fall:

$$\left|Q - Q'\right| \le \varepsilon_Q \ . \tag{24}$$

In the case Eq. (24) does not hold, the distribution $\left(v'_{x2}(r)\right)^2$ is shifted by a constant, which ensures the fulfillment of Eq. (22), and the continuity criterion is checked again. The iterative procedure continues until a valid downstream velocity distribution is obtained.

(v) Integrated energetic relations:

$$\tau = \int_{r_{\text{hub}}}^{r_{\text{tip}}} Z r_i \delta f_{\theta,i_{\text{CIF}}} \ , \tag{25}$$

$$P = \tau\omega \ , \tag{26}$$

$$\Delta p = \frac{\int_{r_{\text{hub}}}^{r_{\text{tip}}}\left(\frac{\rho_a c_i Z C_{x,i_{\text{CIF}}} v_{x1,i}^2}{4\pi r_i \sin\beta_{1,i}^2} + \frac{1}{2}\rho_a\left(v_{1,i}^2 - v_{2,i}^2\right)\right)2\pi r\mathrm{d}r}{\int_{r_{\text{hub}}}^{r_{\text{tip}}} 2\pi r\mathrm{d}r} \ . \tag{27}$$

(vi) Actuator-disk implementation: the actuator-disk theory states that the axial velocity at the disk ($v_{xd,i}$) is the average of the axial components upstream and downstream:

$$v_{xd,i} = \frac{1}{2}\left(v_{x1,i} + v_{x2,i}\right) \ . \tag{28}$$

Once $v_{xd}(r)$ is computed, the calculations from Eqs. (8) to (27) are repeated, i.e. a second iteration is performed upon the BEM approach. The obtained power and pressure drop are then compared to the values retained from the previous step, and checked whether the differences lie below predefined threshold values, thus ensuring energy convergence. Subscripting with j the energetic outcomes of the current iteration, and with $j-1$ the ones of the previous step:

$$\left|P_j - P_{j-1}\right| \le \varepsilon_P \ \wedge \ \left|\Delta p_j - \Delta p_{j-1}\right| \le \varepsilon_{\Delta p} \ . \tag{29}$$

In the case the energy criterion does not hold, $v_{xd}(r)$ is recomputed by considering the current velocity distributions $v_{x1}(r)$ and $v_{x2}(r)$, and going through the BEM subroutine once again. The iterative cycle halts when Eq. (29) is fulfilled. Fig. A.1 illustrates the implementation of the model that combines BEM/actuator-disk approaches.

The outcome of the analytical model is usually provided in terms of dimensionless variables: the flow coefficient given in Eq. (7), and the power (Π), pressure-drop (Ψ) and efficiency (η) coefficients:

$$\Pi = \frac{P}{\rho_a\omega^3 D_{\text{tip}}^5} \ , \quad \Psi = \frac{\Delta p}{\rho_a\omega^2 D_{\text{tip}}^2} \ , \quad \eta = \frac{\Pi}{\Psi\Phi} \ , \tag{30}$$

Table 1
Input parameters of the monoplane Wells turbine employed for sanctioning the validation of the in-house BEM/actuator-disk code, after Ciappi (2020).

Param. type	Parameter	Value(s)
Geom. params.	Z	7 [–]
	r_{cas}	0.5 [m]
	ν	0.75 [–]
	t	1 [%]
	c	0.117 [m]
	Airfoil	NACA0015 [–]
Oper. params.	ω	3600 [rpm]
	$\Phi_{1,\dots,M}$	$\Phi \in [-0.2, 0.2]$
Flow. params.	p_a	101 325 [Pa]
	ρ_a	1.225 [kg/m^3]
	μ_a	1.81×10^{-5} [kg/ms]

being D_{tip} the diameter at the tip. The validation of the BEM/actuator-disk approach has been carried out by comparing the dimensionless outcome curves of a turbine whose specifications are given in Table 1. Results of the validation shown in Fig. 2, with Figs. 2(a) to 2(c) showing the $\Pi - \Phi$, $\Psi - \Phi$ and $\eta - \Phi$ curves, respectively. As observed, the agreement between the in-house analytical code and the one developed in Ciappi (2020) is almost perfect, especially for the $\Pi - \Phi$ and $\Psi - \Phi$ curves. The marginal deviations observed in those variables are mainly due to the different flow parameters imposed, which are considered constant in the present case but are said to be variable in the addressed reference, although such a variation is unspecified. Those deviations are shown to amplify slightly for the efficiency, as may be deduced from Eq. (30), although the deviation remains very low.

The comparisons with a set of unsteady $k-\omega$–based RANS simulations carried out in Ciappi (2020) serve to show the limitations of the analytical approach. As observed, the qualitative agreement is sound, but the analytical approach seems to overestimate the power for the overall operational range, and the same occurs for the pressure drop except for large flow coefficient values. It is to notice, likewise, that the simulations also lie above the experimental data-set obtained in Bassetti et al. (2013) for the same turbine, although the mismatch is smaller than for the analytical case. The comparison of the efficiency curves reveals, once again, that the different Π and Ψ evolution get reflected on the η variable and that, in the case of the CFD simulations, such values are noticeably lower because of the overall lowering of the Π curve, whereas the Ψ values do not change as much.

The observed differences are likely to stem from a number of sources:

- The simplifying assumptions of the analytical model are many. In particular, the semi-3D approach undertaken herein does not devise the interactions between different blade elements, which may turn relevant at moderate Φ values for which the angles-of-attack of the certain radial sections lie close to stalling. It is known that stalling induces inherently three-dimensional fluid structures, which may not be properly captured with the employed model. However, the complexity of the stalling phenomenon is equally challenging for the CFD simulations, which may stand behind the differences observed between the analytical–numerical and the experimental data-sets.
- The incompressibility of the working fluid is also assumed, but compressible effects may become significant when operating at high rotational speeds, especially at the tipward sections of the blades.
- The modeling of certain aerodynamic effects is based on semi-empirical approaches. It is the case of the interference factor (Eqs. (12) and (13)) or the induced drag coefficient (Eq. (10)), whose specific models are provided in Raghunathan (1995). In contrast to the effects stemming from the stalling phenomenon, which affect both the analytical and the CFD results, the semi-empirical models mentioned herein are restricted to the analytical code. The CFD approach reproduces such effects in the simulations, without needing to rely on an independent formulation. On this respect, such semi-empirical models may constitute one of the major contributors to the observed discrepancies between the analytical and CFD data-sets.
- The aerodynamic coefficients upon which the computation of the characteristic curves depends are obtained from the XFoil code (Drela, 1989). XFoil has been validated as a fast computation technique for acquiring such coefficients and, on such a respect, it complies with the underlying philosophy of the analytical approach developed herein. However, its main shortcoming is that it does not model the behavior of airfoils accurately beyond the range within which the lift coefficient of the airfoil varies linearly with the angle-of-attack. This constitutes an additional, potential error source that adds up to the discrepancies observed.
- Sources other than purely aerodynamic ones, such as mechanical losses that ensue on the experimental set-up, may induce differences between the simulated and the tested results. Models for mechanical losses have the additional complexity of being dependent on the specific experimental set-up on which the turbine configurations are tested, which turns the task of including them

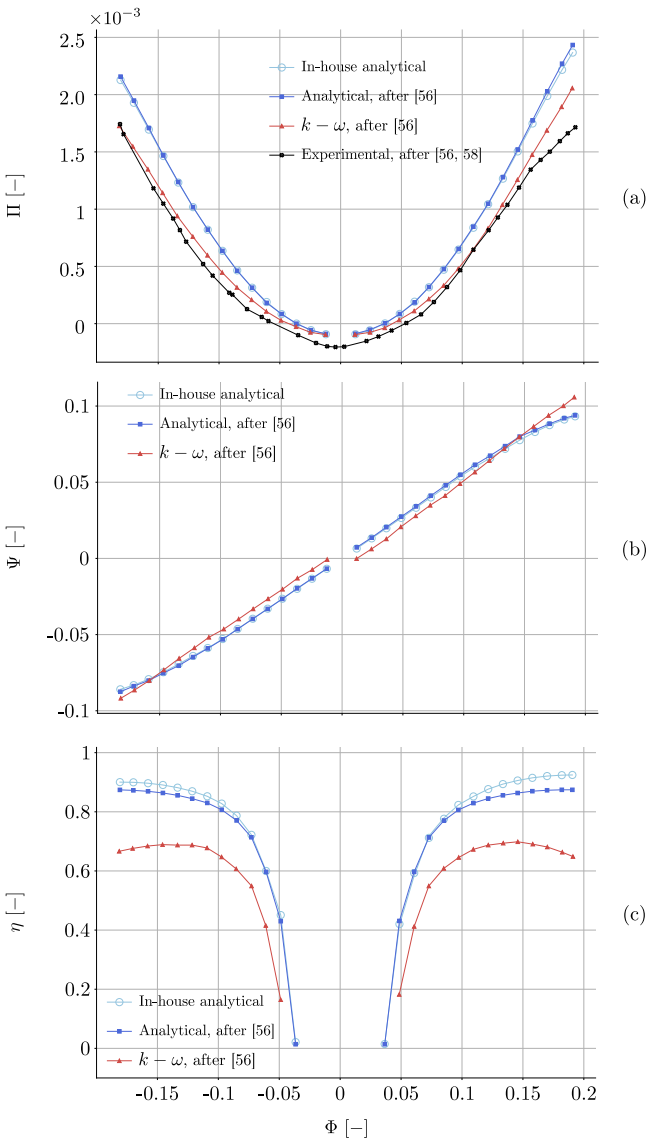

Fig. 2. Validation curves for the in-house analytical BEM/actuator-disk code.

in an analytical model much more challenging or, in the present case, unfeasible.

The caveats mentioned above are relevant for two main reasons. First, they show that the expected results are prone to overestimate both the power and the efficiency of the turbine. When analyzed in terms of the potential error sources discussed above, it may be deduced that such an overestimation comes from the interference factor, which is directly proportional to the square of the local solidity, i.e. σ_i^2. On this respect, larger solidity values will correlate with higher torques and pressure drops, which would induce wider differences with respect to experimental and CFD baseline cases.

Second of all, it shows that there is room for improving the analytical model. Indeed, the code may be modified by implementing corrections derived from CFD- or experiment-related data, although such an approach lies out of the scope of the present paper. In any case, the main focus of the present study is the holistic GA-based optimization approach, which is directly applicable to any update/improvement of the analytical model.

Besides, and apart from the mentioned caveats, it is to mention that the main advantage of the analytical approach is its efficiency in terms of time-resources. The time required for computing the characteristic curves of a turbine configuration by means of the analytical tool lies close to $\mathcal{O}(10)$ seconds, which may be 3 to 4 orders of magnitude below from a CFD approach (Ciappi, 2020), and allows saving the time needed for setting-up the experimental facility, testing the desired configuration and post-processing the data.

2.2. Sea-state variability: stochastic modeling of wells turbines

The stochastic variability of ocean waves affects the distribution of the air pressure in the OWC chamber and, as a consequence, the behavior of a Wells turbine. In order to account for such a stochastic behavior of the Wells turbine, the BEM/actuator-disk model has been extended first by Falcão and Rodrigues (2002) and, more recently, by Falcão et al. (2018) and Alves et al. (2021).

The main assumptions are: (i) the constancy of the rotational speed ω; and (ii) the Gaussian nature of the wave-driven pressure oscillation in the OWC chamber, whose mean and standard deviation are denoted by p and σ, respectively. Following Falcão et al. (2018), the second assumption leads to the following probability density function (PDF) of p:

$$f(p) = \frac{1}{\sqrt{2\pi}\sigma}\exp\left(-\frac{p^2}{2\sigma^2}\right) . \tag{31}$$

With the stochastic nature of the sea-state (SS) being expressed by the PDF above, the averaged values of the air flow rate (Q), the power output (P), and the pneumatic power available to the turbine ($P_{\text{av.}} = pQ$) are given by:

$$\left\{\overline{Q}(\sigma), \overline{P}(\sigma), \overline{P}_{\text{av.}}(\sigma)\right\} = \frac{1}{\sqrt{2\pi}\sigma}\int_{-\infty}^{\infty}\exp\left(-\frac{p^2}{2\sigma^2}\right)\left\{Q(p), P(p), P_{\text{av.}}(p)\right\}\mathrm{d}p , \tag{32}$$

which, in dimensionless variables, adopt the form:

$$\left\{\overline{\Phi}(\sigma_\Psi), \overline{\Pi}(\sigma_\Psi), \overline{\Pi}_{\text{av.}}(\sigma_\Psi)\right\} = \frac{1}{\sqrt{2\pi}\sigma_\Psi}\int_{-\infty}^{\infty}\exp\left(-\frac{\Psi^2}{2\sigma_\Psi^2}\right)\left\{f_\Phi(\Psi), f_\Pi(\Psi), \Psi f_\Phi(\Psi)\right\}\mathrm{d}\Psi , \tag{33}$$

showing that the computation of the stochastic curves results from a convolution of the corresponding variables with the Gaussian PDF. Besides, $f_\Phi(\Psi)$ and $f_\Pi(\Psi)$ represent the functional relations between $\Phi - \Psi$ and $\Pi - \Psi$, respectively, for a range of input velocities upon which the stochastic analysis is computed. The dimensionless variables shown above are defined as:

$$\overline{\Phi} = \frac{\overline{Q}}{\omega D_{\text{tip}}^3} , \quad \overline{\Pi} = \frac{\overline{P}}{\rho_a \omega^3 D_{\text{tip}}^5} , \quad \overline{\Pi}_{\text{av.}} = \frac{\overline{P}_{\text{av.}}}{\rho_a \omega D_{\text{tip}}^5} , \tag{34}$$

with $\sigma_\Psi = \sigma/\rho_a\omega^2 D_{\text{tip}}^2$ being the dimensionless counterpart of the pressure oscillation p. Similarly, the average efficiency is:

$$\overline{\eta}(\sigma_\Psi) = \frac{\overline{\Pi}(\sigma_\Psi)}{\overline{\Pi}_{\text{av.}}(\sigma_\Psi)} . \tag{35}$$

On practical grounds, the convolution integral is calculated by replacing the infinite limits with a finite value of the dimensionless pressure-drop coefficient, $\Psi_{\max}$, which constitutes an input to the calculations.

The workflow that corresponds to the stochastic calculations is illustrated in Fig. A.2.

3. Definition of optimization strategy and case-study

The optimization strategy of the current study comprises (i) the collection of geometrical parameters that have an influence on the behavior of a Wells turbine, which are presented in Section 3.1; (ii) the assessment of the holistic behavior of the WEC, including the hydrodynamic and pneumatic effects of the device, the aerodynamic behavior of the turbine, and the control action and constraints that act upon the turbine configuration and delimit the parametric space, as described in Section 3.2; and (iii) the varying wave conditions so that the optimization is undertaken under realistic wave climate conditions, which is given in Section 3.3. The flowchart illustrated in Fig. 3 represents the workflow of the optimization methodology presented in this study and further described in the following subsections. Finally, the novel optimization method suggested in this paper is aided by a parallelized GA algorithm in order to reduce the number of evaluations, avoiding the need to analyze the whole search space.

3.1. Definition of the parametric space

The set of geometrical parameters that are subjected to the optimization algorithm comprise:

- The number of blades: Z.
- The hub-to-tip-ratio: ν.
- The solidity at the hub: σ_{hub}.
- The solidity at the tip: σ_{tip}. Assuming a linear variation of the chord in the spanwise dimension, namely $c(r) = a + br \ \forall r \in [r_{\text{hub}}, r_{\text{tip}}]$, the pair $(\sigma_{\text{hub}}, \sigma_{\text{tip}})$ determines the duple (a, b) of the chordal distribution, as:

$$a = \frac{2\pi\nu r_{\text{tip}}(\sigma_{\text{tip}} - \sigma_{\text{hub}})}{Z(\nu - 1)} \tag{36}$$

$$b = \frac{2\pi(\nu\sigma_{\text{hub}} - \sigma_{\text{tip}})}{Z(\nu - 1)} \tag{37}$$

  which includes the constant-chord configurations as particular cases $(b = 0 \Rightarrow \sigma_{\text{tip}} = \nu\sigma_{\text{hub}})$.
- Tip clearance percentage: $\mathfrak{t}$.
- The number of different airfoil geometry distributions along the span, together with the airfoil geometries corresponding to such distributions. It has been decided to constrain the possible spanwise distribution of airfoil geometries into a set of three most commonly used NACA shapes, namely the NACA0015, NACA0018 and NACA0021 ones (Starzmann and Carolus, 2014; Ciappi et al., 2020). Likewise, the span of the blade is divided into three equal regions, each of which being allowed to adopt any of the mentioned airfoil geometries. As such, the overall amount of combinations rises to 27 different possibilities.

In the case of the operational parameters, the rotational speed of the simulations, namely 2100 rpm, is set at the average value of the limits imposed for the computation of the fitness value, i.e. $[\omega_{\min}, \omega_{\max}] = [1000, 3200]$ rpm, and the range of inflow coefficients is extended when compared to the validation case, covering the interval $\Phi_1 \in [0, 0.16]$. Both the geometrical and the operational parameters for the optimization are gathered in Table 2.

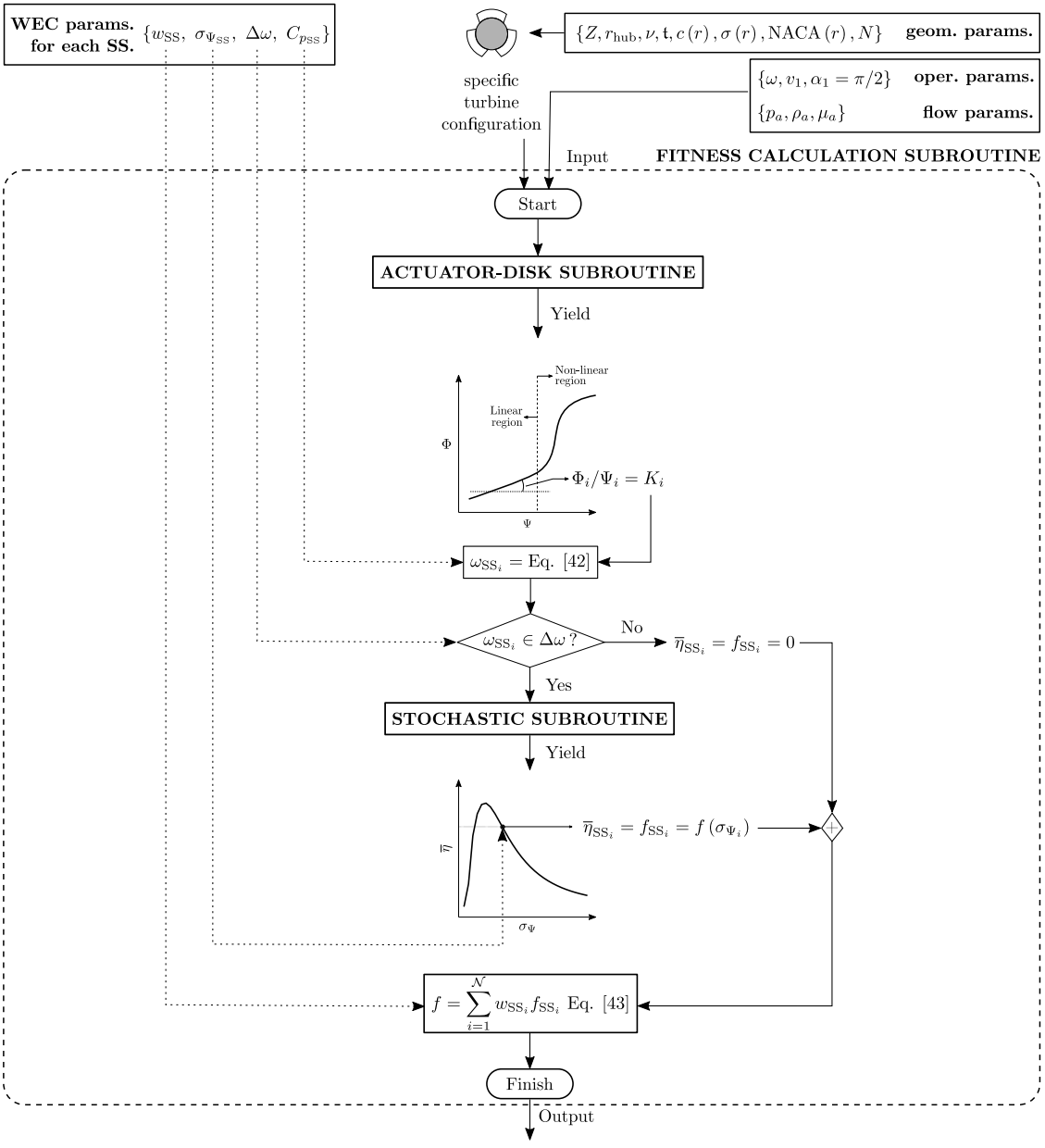

Fig. 3. Flowchart of the fitness calculation subroutine.

Table 2
Set of geometrical and operational parameters for the sea-state-pondered optimization of Wells turbines.

Param. type	Parameter	Value range	# of values
Geom. params. to optimize	Z	$Z \in [3, 7]$ [–]	3
	σ_{hub}	$\sigma_{hub} \in [0.4, 0.7]$ [–]	10
	σ_{tip}	$\sigma_{tip} \in [0.4, 0.7]$ [–]	10
	ν	$\nu \in [0.4, 0.75]$ [–]	10
	$\mathfrak{t}$	$\mathfrak{t} \in [0.5, 3]$ [%]	10
	Spanwise airfoil distribution	Span divided into three equal portions; NACA0015, NACA0018 and NACA0021 airfoils to be chosen.	27
			Total conf. 8.1×10^5
Oper. params.	ω	2100 [rpm]	–
	$[\omega_{min}, \omega_{max}]$	[1000, 3200] [rpm]	–
	$\boldsymbol{\Phi}_{1_{i,\ldots,M}}$	$\boldsymbol{\Phi}_1 \in [0, 0.16]$	–

3.2. Definition of the fitness function

The calculation of a particular turbine configuration's fitness value proceeds thusly:

- The dimensionless characteristic curves of the turbine are obtained by means of the BEM/actuator-disk subroutine, considering a constant rotational speed of $\omega_0 = 2100$ rpm and a set of inflow velocities $\Phi_1 \in [0, 0.16]$.
- An advantage of the dimensionless curves is that they are independent of the operation parameters and flow variables. Wells turbines, in particular, are known to have a $f_\Phi(\Psi)$ relation that is linear (Falcão and Henriques, 2016), namely:

$$\Phi = K\Psi \ . \tag{38}$$

Thus, even if the turbine curves have been obtained for a particular rotational speed ω_0, Eq. (38) can be employed for determining the actual speed ω_{SS} at which the turbine operates when facing a given sea-state (SS). By dimensional analysis, the constant K can be inferred to follow the expression below:

$$K = \frac{\rho_a \omega_{SS}}{D_{tip} C_{p_{SS}}} \ , \tag{39}$$

where the $C_{p_{SS}}$ variable is called the damping coefficient of the turbine, which represents the control action imposed from the generator and constitutes an input value that depends on the sea-state (Falcão, 2002). Having computed the value of K from a linear fitting of the stochastic relationship $f_\Phi(\Psi)$ given by Eq. (38), and knowing the optimal $C_{p_{SS}}$ that corresponds to each sea-state, the value of ω_{SS} is obtained straightforwardly:

$$\omega_{SS} = \frac{D_{tip} C_{p_{SS}} K_{fit}}{\rho_a} \ , \tag{40}$$

with K_{fit} indicating that its value stems from the mentioned linear fitting of $f_\Phi(\Psi)$.

- The value of ω_{SS} is checked against the operational constraints that define the admissible rotational speed range of the turbine, which is denoted as $[\omega_{min}, \omega_{max}]$. If $\omega_{SS} \notin [\omega_{min}, \omega_{max}]$, then the fitness ($f_{SS}$) of the configuration subjected to such a sea-state is set to a null value, $f_{SS} = 0$.
- Otherwise, the stochastic dimensionless curves of the turbine are computed. Knowing the standard deviation of the pressure oscillation in the OWC chamber that corresponds to the sea-state SS, namely $\sigma_{\Psi_{SS}}$, the fitness value of the configuration is set to the stochastic efficiency that corresponds to such a deviation, i.e. $f_{SS} = \overline{\eta}|_{\sigma_\Psi = \sigma_{\Psi_{SS}}}$. The standard deviation is specifically computed for each sea-state under a specific control action based on JONSWAP irregular waves (Hasselmann et al., 1973). For the case-study analyzed herein, which is detailed in Section 3.3, those deviations have been obtained by means of a wave-to-wire model of the MARMOK-A-5 device.

The procedure described above, depicted in Fig. 3, serves for calculating the fitness value of an individual turbine configuration that is subjected to a single sea-state. However, the approach of the present work considers a set of different sea-states, which are leveled in accordance to their occurrence probability. Such probabilities are provided as input weights, i.e. $\left[w_{SS_1}, \ldots, w_{SS_\mathcal{N}}\right]$, $\mathcal{N}$ being the number of sea-states considered in the optimization. Accordingly, the input damping control parameters and standard deviations are provided as arrays, namely $\left[C_{p_{SS_1}}, \ldots, C_{p_{SS_\mathcal{N}}}\right]$ and $\left[\sigma_{\Psi_{SS_1}}, \ldots, \sigma_{\Psi_{SS_\mathcal{N}}}\right]$, respectively. The overall fitness value corresponds to a weighted average of the stochastic efficiencies obtained for each sea-state, which results in a sea-state-pondered optimization:

$$f = \sum_{i=1}^{\mathcal{N}} w_{SS_i} f_{SS_i} \ . \tag{41}$$

Table 3
Case-study parameters for the sea-state-pondered optimization of Wells turbines.

	Sea state # (SS)	$C_{p_{SS}}$ [–]	$\sigma_{p_{SS}}$ [Pa]	ω_{SS} [%]
Sea-state params.	1	934	2171	10.85
	2	1089	2852	11.6
	3	1089	2932	11.88
	4	1012	2782	9.1
	5	1012	2542	8.24
	6	1012	4519	14.86
	7	934	4087	8.82
	8	934	3806	8.67
	9	934	5846	9.45
	10	856	6745	6.52

3.3. Definition of the case study

As mentioned in Section 1, the realistic case-study considered herein is inspired by the spar-like floating OWC device MARMOK-A-5 (Weller et al., 2017; Carrelhas et al., 2019) developed by IDOM, which was deployed at the Biscay Marine Energy Platform (BiMEP) test-site (BIMEP, 2022) for over two and a half years. For this study, the system is defined as a monoplane Wells turbine owning a 1-meter diameter casing ($r_{cas} = 0.5$ m), which is considered a frozen variable of the configuration for the following optimization. The realistic wave climate conditions have been reduced to the 10 most probable sea-state cases, whose determining parameters are gathered in Table 3. However, it should be noted that turbine diameter can also be included in the optimization and that the number of sea-states can also be adapted according to the characteristics of each geographical location.

4. Results and discussion

The presentation of the results proceeds as follows: Section 4.1 analyzes the turbine configurations with the highest fitness values, thus identifying the most relevant geometrical parameters influencing the behavior of the device. This first campaign is termed as "coarse optimization", meaning that the overall parametric space is considered in the searching process, with the aim of determining the parametric regions for which the fitness achieves the highest values. Such an identification allows constraining the searching space by getting rid of the least relevant parameters. Undertaking the analysis upon such a reduced landscape in a searching procedure that has been termed as "refined optimization" leads to insights of a more physical meaning as explained in Section 4.2, ultimately permitting to achieve a representative map of the turbine's fitness evolution.

As the results are meant to show the outcome of a GA-based optimization process, the parameters of such an algorithm have been tuned by means of undertaking a convergence study following the guidelines in Pourrajabian et al. (2021), which applies a similar optimization strategy upon airfoil blades. The convergence study comprises different population sizes, generation numbers and mutation rates, apart from considering variations in the implemented operators. The chosen GA configuration fixes both the population size and the number of generations to 160, imposes a mutation rate of 5% and employs the uniform crossover operator. The convergence rate lies above 99.95%, meaning that deviations from the global maximum are expected in 0.05% of the optimization runs. Finally, the GA algorithm has been parallelized, achieving an average CPU time of between 15-30 min for the whole optimization procedure.

4.1. Coarse optimization

Based on the GA configuration defined above, Table 4 shows the best 10 cases obtained with the mentioned GA configuration. As

Table 4
Optimized parameter values for the GA trial showing the highest fitness value with the best convergence rate.

Z	σ_{hub}	σ_{tip}	ν	NACA dist.			t	f
				Root	Mid	Tip		
3	0.7	0.633	0.478	NACA0015	NACA0015	NACA0021	0.5 0.778 1.056 1.333 1.611 1.889 2.167 2.444 2.772 3	0.526

Table 5
Optimized parameters for the first three best cases.

Config.	Z	σ_{hub}	σ_{tip}	ν	NACA dist.			f
					Root	Mid	Tip	
I	3	0.7	0.633	0.478	NACA0015	NACA0015	NACA0021	0.526
II			0.6	0.517				0.525
III			0.667	0.439				0.522

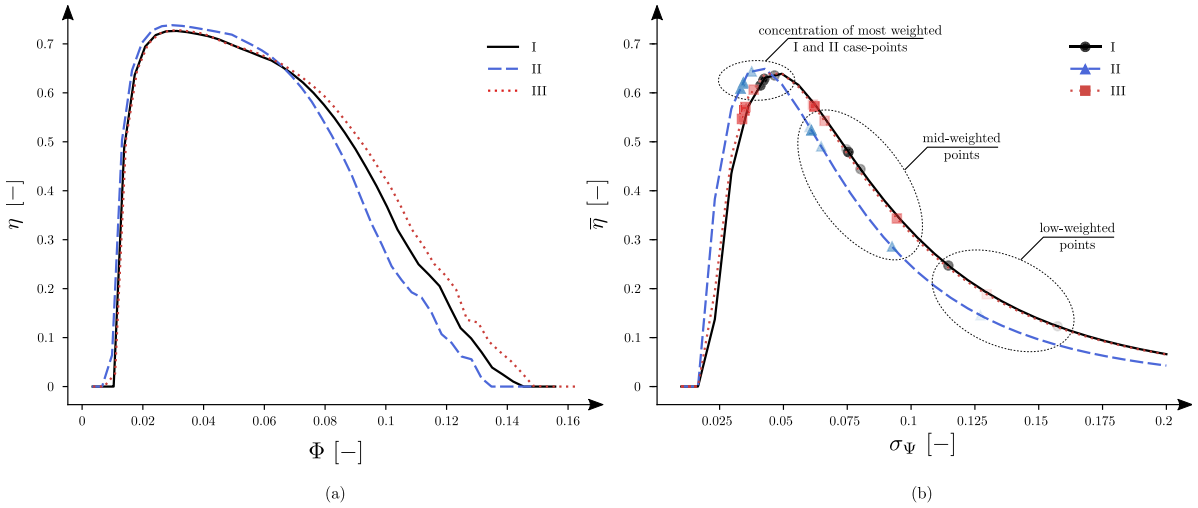

Fig. 4. Efficiency curves for the best three cases shown in Table 5; (a) non-stochastic $\Phi - \eta$ curves; (b) stochastic $\sigma_\Psi - \overline{\eta}$ curves.

observed, the only geometrical parameter that shows any variance is the tip clearance t, which shows all the possible values it can achieve according to Table 2. Furthermore, the overall set of best configurations shows the same fitness value. This means that, on the basis of the stochastic efficiency curves employed for computing the fitness value, the tip clearance itself does not induce any relevant change. On this respect, what Table 4 provides is an assertion that it is possible to reduce the dimensionality of the parametric space by taking the tip clearance variable out of the analysis.

Indeed, Table 5 shows the best three cases for the same GA configuration run upon the 5-dimensional parametric space that results from fixing the tip clearance parameter to a value of 0.5%. In this case, the differences in the fitness value become evident, which corroborates the fact that the tip clearance constitutes a secondary geometrical parameter on the design process. Additionally, it is possible to carry out the same analysis as when interpreting Table 4, and to deduce that the set $(Z, \sigma_{hub}, \text{NACA}_i)$ is of lesser importance than the pair (σ_{tip}, ν) in determining the fitness value of the best cases. However, that would be a misleading conclusion. The set $(Z, \sigma_{hub}, \text{NACA}_i)$ does influence the final value of the computed fitness, although such an effect starts to become apparent beyond the 4th case owning the highest fitness value. Instead, the irrelevance of the tip clearance parameter when it comes to the computation of the current fitness function gets manifest in each of the three best cases represented in Table 5. In other words: were each of such cases projected onto the dimensional space of the tip clearance parameter, the 10 resultant configurations would yield the same fitness value as occurred when analyzing the data in Table 4, a task which has not been carried out herein for the sake of conciseness.

Apart from the fitness values themselves, it is illustrative to compare the efficiency curves of the configurations in Table 5 for gaining insight on the optimized turbine behaviors. Such is the purpose of the plots shown in Fig. 4, where Fig. 4(a) represents the non-stochastic $\Phi - \eta$ curves, whereas Fig. 4(b) shows the stochastic $\sigma_\Psi - \overline{\eta}$ ones. Both plots share the same scale on the vertical axis for comparative purposes, although the curves whereby the fitness values get computed are the ones in Fig. 4(b). As observed, little can be said based on the $\Phi - \eta$

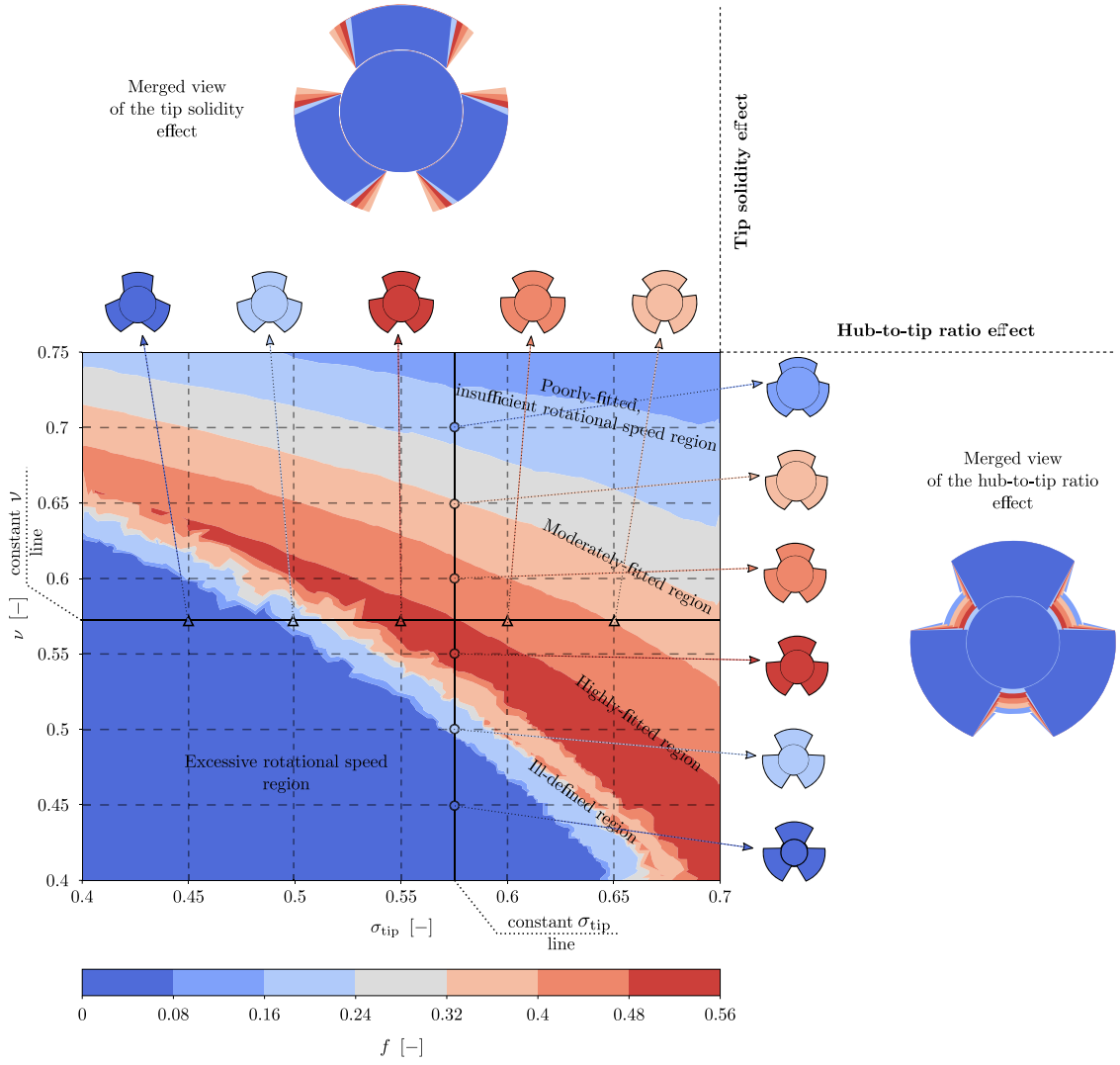

Fig. 5. Fitness contour map for the refined optimization based upon the 2-dimensional parametric space of (σ_{tip}, ν).

curves: morphologically they look similar apart from the relatively premature drop in efficiency of the configuration II, although it is the curve that shows the largest efficiency peak at low Φ values, even if such a peak dominates marginally. Besides, the best behavior at large flows is that of configuration III; configuration I, on this respect, shows an intermediate performance with respect to its counterparts.

The situation changes when analyzing the curves in Fig. 4(b). Indeed, the points corresponding to each of the sea-states are represented with a progressive fade that is representative of the weight or contribution of such a sea-state to the overall fitness value. Stronger points refer to higher weights, whereas faded points correspond to lower ones. The first thing to notice is that the peak stochastic efficiencies lie sensibly below their non-stochastic counterparts, which is an effect of the convolution operation expressed in Eq. (33); this is more notable in the case II curve, whose previously mentioned premature drop in the $\Phi-\eta$ plot gets reflected on an overall leftwards shift of the $\sigma_\Psi - \overline{\eta}$ curve. The second relevant point is that the most weighted sea-states of the cases I and II get clustered around the peak of the stochastic efficiency, whereas the mid- and low-weighted points are more distributed along the moderate-to-high σ_Ψ values. Instead, the most weighted points of case III fall perceptibly below its corresponding curve peak, which leads to the ultimate fitness value showing a lower value altogether. Hence, the algorithm attempts at finding the turbine configurations whose sea-state-related efficiencies best distribute around the peak, to the cost of relegating the mid- and low-contributing sea-states to low efficiency values.

4.2. Refined optimization

Even if the analysis provided in Section 4.1 serves the purpose of gaining insights into the behavior of the turbines with the highest fitness values, the research may proceed by refining the search around the best configurations shown in Table 5. Indeed, as mentioned before, the set $(Z, \sigma_{tip}, \text{NACA}_i)$ adopts the same values for such three cases and, therefore, it means that it is possible to discard those three parameters for performing a finer sampling upon the resultant dimensional space. If such an approach is adopted, the overall space is reduced to a 2-dimensional map comprising the parameters (σ_{tip}, ν). As shown in the cited work of Pourrajabian et al. (2021), a GA configuration running over continuous gene values is more efficient in finding the individuals with the highest fitness than its discrete-valued counterpart. Unlike for the general 6-dimensional case, the volume reduction of the parametric space to the 2-dimensional case turns feasible the fact of launching a GA upon the continuous (σ_{tip}, ν) map.

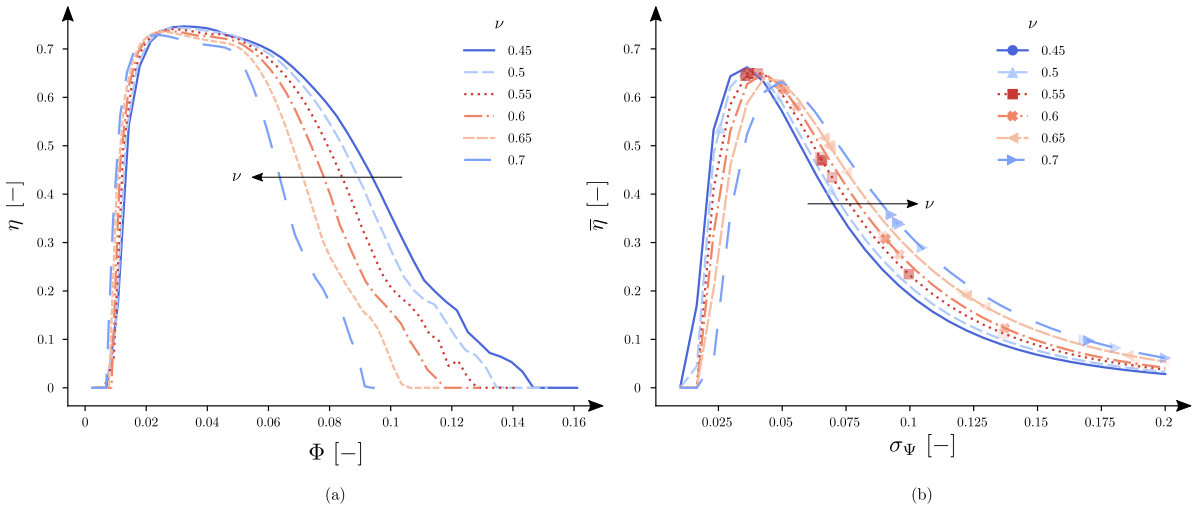

Fig. 6. Efficiency curves showing the effect of ν on the turbine behavior for a fixed value of $\sigma_{tip} = 0.575$; (a) non-stochastic $\Phi - \eta$ curves; (b) stochastic $\sigma_\Psi - \overline{\eta}$ curves.

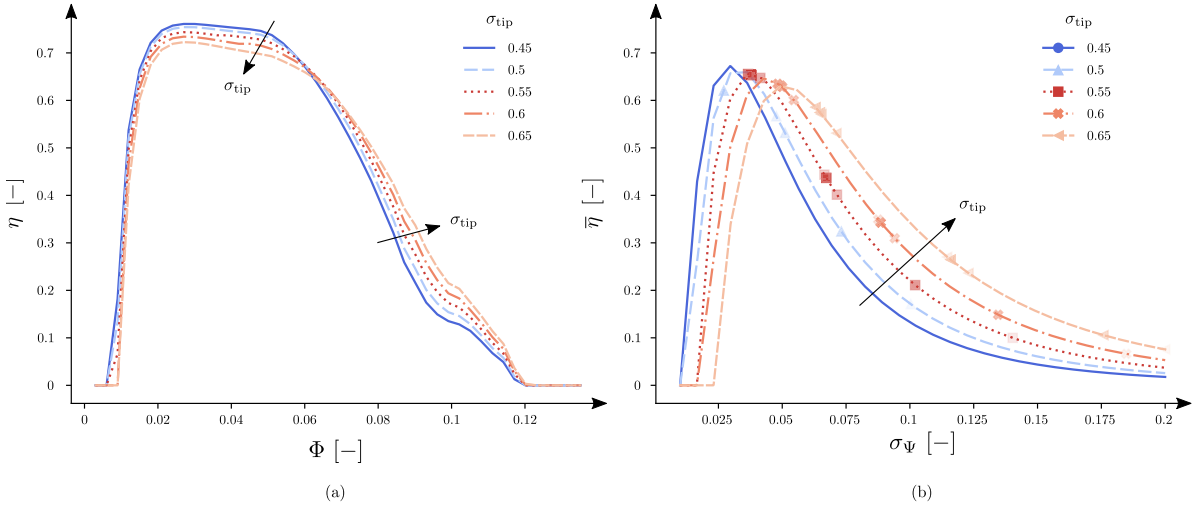

Fig. 7. Efficiency curves showing the effect of σ_{tip} on the turbine behavior for a fixed value of $\nu = 0.575$; (a) non-stochastic $\Phi - \eta$ curves; (b) stochastic $\sigma_\Psi - \overline{\eta}$ curves.

Mind that the mentioned reduction is different from the one performed when discarding the influence of the tip clearance parameter. In such a case, the reasoning was that the parameter itself did not affect the fitness outcome at any relevant level. The argument for reducing the 5-dimensional space to the 2-dimensional one is that getting rid of the extra 3 parameters allows refining the search upon a previously constrained set of configurations, not that the discarded parameters do not affect the fitness value altogether. At most, it is reasonable to assert that such parameters do not affect the outcome at a neighborhood of the global maximum. Besides, the overall map on the 5-dimensional hyperspace would match the 6-dimensional one, showing the irrelevance of considering the tip clearance as a design parameter on the basis of the proposed fitness function.

Fig. 5 depicts the contour map of the fitness function on the 2-dimensional (σ_{tip}, ν) interval established in Table 2. As observed, launching the GA upon such a continuous interval provides a map where it is possible to identify multiple, well-delimited regions. A full understanding of the information contained in such a map requires the complementary help of the efficiency curves represented in Figs. 6 and 7, which match the layout of the data provided in Fig. 4.

Those efficiency curves correspond to specific turbine configurations sampled from the 2-dimensional map shown in Fig. 5. In particular, the curves in Fig. 6 refer to the turbine designs that result from keeping the tip solidity constant at a value of $\sigma_{tip} = 0.575$; the family of resultant turbine configurations is represented by the vertical solid line in Fig. 5. For illustrative purposes, the specific designs chosen for the comparative task are those whose hub-to-tip ratios coincide with the vertical axis ticks. Such specific designs are identified by circular symbols in the map and, as observed, they fall in qualitatively different regions of the fitness contour. The sketches at the right hand-side of the map represent the front views of the chosen turbine configurations, and are colored in accordance to the map region they lie on. The rightmost

sketch stands for a merged view of such turbine configurations, and is plotted with the aim of easing the comparison among the different designs resulting from the varying value of ν.

Likewise, the curves in Fig. 7 represent the counterpart of the hub-to-tip ratio effect, focusing on the σ_{tip} parameter instead. The corresponding family of turbine designs, once having fixed a value of $\nu = 0.575$, is reduced to the ones falling upon the horizontal solid line of the 2-dimensional map. The specific designs chosen for comparative purposes are identified with triangular symbols and, in compliance with the previous procedure, they fall within qualitatively different regions of the fitness contour. The sketches of their respective front views are plotted at the top of the map, with the corresponding merged view located above them.

Having described the layout of Figs. 5 to 7, each of the parametric effects may be discussed independently, with the purpose of establishing their common features and differences.

- **Hub-to-tip ratio effect:**
  Fig. 6(a) shows a progressive shortening on the range of effective flow coefficients with increasing values of ν, meaning that larger hub-to-tip ratios lead to narrower non-stochastic efficiency curves along the Φ-axis. Such a reduction on the effective operational flow range is related to the features of the turbine design; as observed in Fig. 5, increasing the hub-to-tip ratio for a constant σ_{tip} produces turbines with a larger hub and smaller blade areas. Consequently, the turbine itself requires higher incoming flows for overcoming the blockage induced by the hub, and the turbine rotates slower. Such a slower rotation correlates with higher angles-of-attack on the blade sections, leading to a promoted stall. To the contrary, turbines with low ν values rotate faster because their smaller blockage, showing a wider efficiency curve as a consequence.
  On the fitness side, Fig. 6(b) shows how those features are translated into the stochastic behavior and, hence, to the overall score that the turbine designs achieve in the GA computation. Notice that the lowest $\nu-$ valued design falls within the poorest fitness region, and that the corresponding stochastic curve does not show any data-points representing the $\overline{\eta}$ value of a sea-state. Given that the GA code is implemented so the sea-states for which the turbine's rotational speed falls outside the interval of predetermined bounds are ascribed a null contribution to the fitness value, the reason for the low-valued zone at the bottom-left of the fitness contour has to do with an excessive rotational speed of those designs. Indeed, insofar such a region corresponds to low values of both ν and σ_{tip} parameters, the resultant designs show a minimal blockage to the incoming flow and, consequently, operate at velocities that fall beyond the upper limit of the predefined rotational speed interval.
  Increasing the hub-to-tip ratio further leads to the so-called ill-defined zone, given the large fluctuations that are observed therein as for the fitness values. A larger ν produces turbines with greater hubs and smaller blades, increasing the blockage accordingly. Hence, certain valid data-points begin to show up on the $\sigma_\psi - \overline{\eta}$ curve, although such points lie relatively apart from the curve's peak.
  The region of highly-fitted turbine configurations corresponds to the designs that achieve a proper trade-off between the blockage induced and the rotational speed. It is straightforward to observe that, for the $\nu = 0.55$ case, the most weighted sea-state data-points fall in the close neighborhood of the corresponding $\sigma_\psi - \overline{\eta}$ curve, which is the reason for the large fitness value shown by the configuration.
  Moving at even larger hub-to-tip ratios progressively leads towards the moderately- and poorly-fitted regions. Those transitions have to do with the increasingly lower rotational speeds of the resultant turbine designs, which show both an increased hub and a decreased blade area that causes an excessive blockage as mentioned before. Such a behavior gets reflected on the gradual spread of the data-points in the $\sigma_\psi - \overline{\eta}$ curves towards the low $\overline{\eta}$ region at high σ_ψ values. Notice that such an effect is not as critical as the excessive speed at which low $\nu-$ valued turbines rotate. Indeed, the designs with $\nu \geq 0.6$ do achieve to operate within the acceptable rotational speed regime, but the operational points themselves get progressively further from the optimal efficiency region.
  Anyhow, the analysis of the hub-to-tip ratio parameter shows that the design philosophy of the turbine configuration with the highest fitness aims at a trade-off solution between the two effects that come into play. Going for low blockages causes the resultant turbines to operate at exceedingly large rotational speeds in order to fulfill the requirements imposed by the sea-states, which may result in vibration and fatigue problems of mechanical origin. To the contrary, aiming at large blockages probably alleviates those issues, but the resultant designs are sub-optimal with respect to the efficiency they provide.
- **Tip solidity effect:**
  The joint interpretation of Figs. 5 and 7 shows certain differences when compared to the analysis of the hub-to-tip ratio parameter. Indeed, the morphology of the curves shown in Fig. 7(a) bear little resemblance to their counterparts on Fig. 6(a).
  Indeed, the peak values of the non-stochastic efficiencies reduce progressively as the σ_{tip} parameter increases, and the trend remains until it is inverted for flow parameter values beyond $\Phi = 0.06$. This has to do, probably, with the relation between the incoming flow, the chord-based Reynolds number at the tip and the corresponding lift and drag curves of the employed NACA airfoils, a relation that is of a purely aerodynamic nature. Assuming that the largest contributions to both the output power and to the losses come from the tipwards regions of the turbine, it may be stated that the morphology of the efficiency curves is equally dictated, majorly, by the aerodynamic behavior of the airfoils located therein. Increasing the σ_{tip} value leads to larger chord dimensions at the tip that, consequently, induce those airfoils to operate at higher Reynolds numbers. In fact, the most critical case corresponding to an incoming flow of 45 m/s shows that the tip-chord-based Reynolds number increases from 2.5×10^6 to 3.6×10^6 between the turbines with the minimum and maximum σ_{tip} values, respectively, which corresponds to a variation of 144%. This difference makes them operate under distinct aerodynamic conditions, and notice that such an effect does not occur in the case of a constant-valued σ_{tip} parameter due to the same chordwise dimension at the tip. Lower Reynolds-numbered aerodynamic curves are known to show relatively larger lift coefficients at low angles-of-attack; such a trend, however, reverts for high angles-of-attack, with the lower Reynolds-valued cases stalling earlier. Such behaviors are being reflected on the $\Phi-\eta$ curve, considering that lower Φ values correlate with smaller angles-of-attack and vice-versa.
  When it comes to the stochastic interpretation of Fig. 7(b), the mentioned aerodynamic effect gets combined with the previously stated blockage effect. As before, the lowest σ_{tip} case falls within the poorly-fitted region due to an excessive rotational speed. Likewise, the configuration standing upon the ill-defined region shows $\overline{\eta}$ data-points that depart noticeably from the maximum efficiency region. However, the rest of the cases, including the one lying on the highly-fitted zone, show a relatively larger scattering of the data-points across the σ_ψ-axis than in Fig. 6(b). Although the transition from highly- to moderately-fitted regions has to do with the increasing blockage effect of augmenting the σ_{tip} value, the spreading of the points is due to the different aerodynamic conditions at which the tipwards airfoils operate. Even if the general conclusions regarding the blockage effect remain, it is

relevant to consider them together with the aerodynamic effect induced by the different chordwise dimensions at the tip.
As mentioned before though, the case with the highest fitness corresponding to the σ_{tip} analysis also stands for a trade-off design philosophy, promoting an intermediate solution between: the low-blocking, prematurely-stalling, small $\sigma_{tip}-$ valued configurations, on the one hand; and the highly-resistant, stall-avoiding, large $\sigma_{tip}-$ valued turbines, on the other hand.

The analysis undertaken has shown that refining the search upon the global maximum by means of reducing the parametric space into a 2-dimensional map allows performing a more detailed study upon the effects induced by the relevant geometrical parameters that influence the turbine design according to the predefined fitness value. The variations on both the hub-to-tip ratio and the tip solidity have been traced back to their physical- and flow-related origins, showing an interplay between blockage-, rotational-speed- and aerodynamics-related effects. On such grounds, the preferred turbine configurations have been shown to constitute a trade-off between the considered geometrical parameters, thus aiming at making the devices operate near the maximum $\overline{\eta}$ point for as much sea-states as possible.

5. Conclusions

A holistic optimization approach for the design of wave energy converters' power take-off systems under realistic wave climates is presented in this paper, which has been applied to floating oscillating water column devices and Wells turbines. To that end, an analytical model for air turbines is developed and incorporated into a GA-based optimization approach that finds the turbine configuration with the highest sea-state-pondered fitness function. The main findings of the work may be summarized as follows:

- The presented workflow is effective in identifying geometrical parameters that are not relevant in terms of the implemented sea-state-pondered fitness function. In particular, the coarse optimization searching has served to determine that the tip clearance parameter is negligible on this respect.
- The search upon a refined 2-dimensional space comprising the (σ_{tip}, ν) doublet allows launching a continuous GA that results in a fitness contour map. The analysis of such a map shows that:
  i. The effect of increasing ν values for a fixed σ_{tip} results in a gradual increment of the turbine's blockage, passing from operating at excessive rotational speeds to working under largely sub-optimal conditions. The blockage effect prevails when considering the hub-to-tip ratio parameter.
  ii. In the case of increasing σ_{tip} values, the mentioned blockage acts in conjunction with the aerodynamic effects coming from a growing chord-based Reynolds number at the tip, which induces a milder fitness loss than when considering the hub-to-tip ratio alone.
  iii. In either case, the preferred turbine configurations comply with the trade-off design philosophy, averaging the blockage, operational speed and aerodynamic effects for making the resultant configuration operate near the peak of the efficiency curve for as many sea-states as possible.

In addition to the mentioned conclusions, it is relevant to advance a number of potential future research lines that have stemmed from the insights gained during the study:

- The analytical formulation is subjected to several simplifications: the lack of a model for capturing the 3D effects stemming from the stalling phenomenon, the incompressibility assumption, the semi-empirical modeling of aerodynamic effects, the XFoil-based aerodynamic coefficients or the absence of mechanical losses. Improving it requires either reformulating the analytical theory itself or to adopt a semi-hybrid approach, be it either incorporating experimental or higher-fidelity numerical results.
- The code can be modified to evaluate turbine architectures such as biplane and counter-rotating configurations, or a basic control procedure for the study of variable-pitch turbines. This would allow computing a multi-configuration optimization study.
- It may be relevant to look for local maxima throughout the parametric space, aiming at dimensional reductions of the (σ_{tip}, ν) type that relate other geometrical parameters in a visual manner.
- The statistical probability of occurrence may not be the best indicator for clustering sea-states. Likewise, a fitness function based on a weighted sum of the stochastic efficiencies might fall short when trying to consider other outcome parameters, such as the losses or the power alone. It is necessary to determine the suitability of such approaches.

Although applied to oscillating water column devices and Wells turbines in the present study, the GA-based optimization method suggested in this study can be extensible to any other wave energy converter that includes a different power take-off system.

CRediT authorship contribution statement

Ander Zarketa-Astigarraga: Conceptualization, Methodology, Software, Validation, Formal analysis, Investigation, Data curation, Writing – original draft, Writing – review & editing, Visualization. **Alain Martin-Mayor:** Conceptualization, Methodology, Resources, Writing – review & editing, Supervision, Project administration, Funding acquisition. **Aimar Maeso:** Conceptualization, Methodology, Resources, Project administration, Funding acquisition. **Borja de Miguel:** Conceptualization, Methodology, Resources, Project administration, Funding acquisition. **Manex Martinez-Agirre:** Conceptualization, Methodology, Resources, Writing – review & editing, Supervision, Project Administration, Funding acquisition. **Markel Penalba:** Conceptualization, Methodology, Resources, Writing – Original draft, Writing – review & editing, Supervision, Project Administration, Funding acquisition.

Declaration of competing interest

The authors state that no conflicts of interests with other institutions have taken place during the elaboration of the submitted manuscript.

Data availability

The authors do not have permission to share data.

Acknowledgments

This publication is part of the research project PID2021-124245OA-I00 funded by MCIN/AEI/10.13039/501100011033 and by ERDF A way of making Europe, the European Union's Horizon 2020 research and innovation EuropeWave programme under the grant No 883751, and the research project funded by the Basque Government's ELKARTEK 2022 program, Spain under the grant No. KK–2022/00090. In addition, the authors from the Fluid Mechanics research group at Mondragon University are also supported by the Basque Government's Research Group Program, Spain under the grant No. IT1505-22.

Appendix. Flowcharts for the analytical implementation

See Figs. A.1 and A.2.

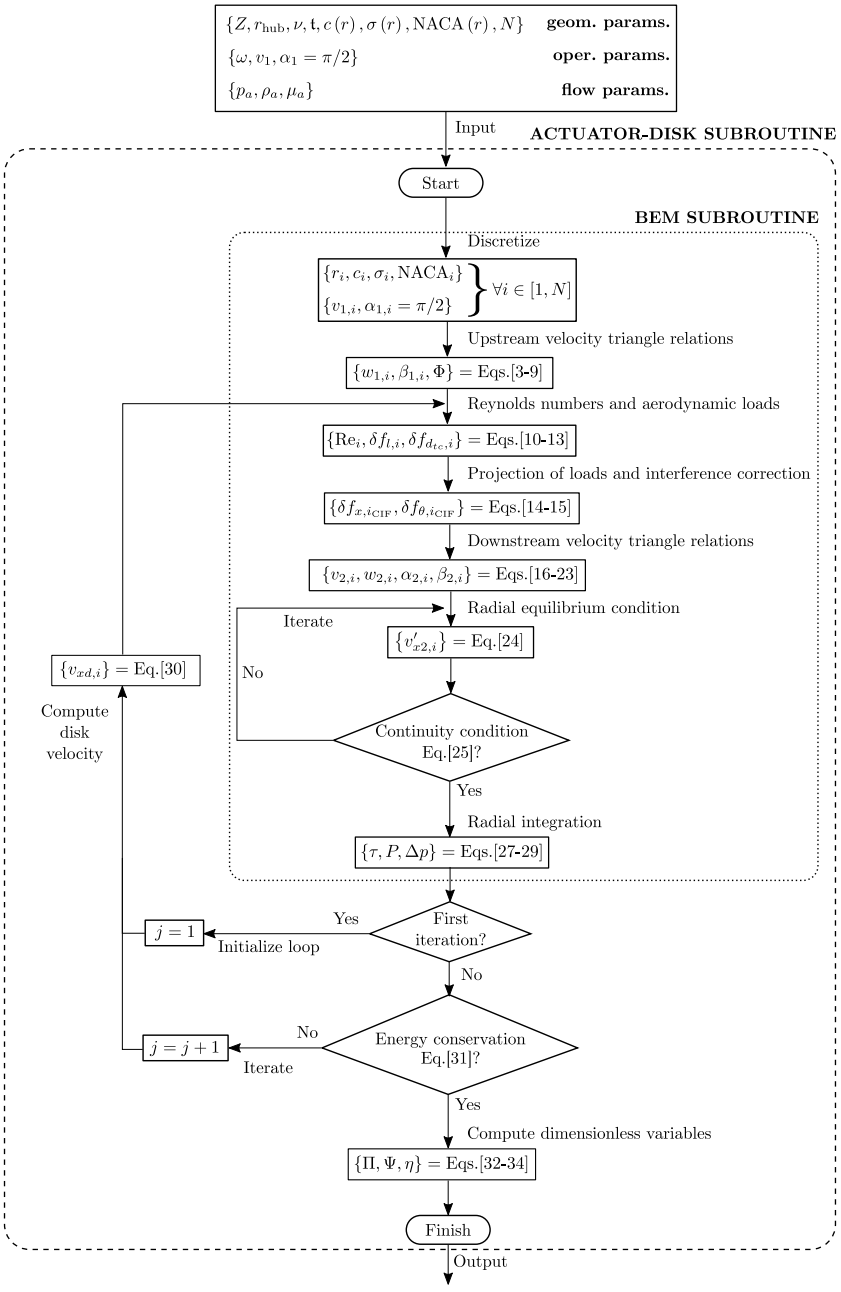

Fig. A.1. Flowchart of the combined BEM/actuator-disk approach.

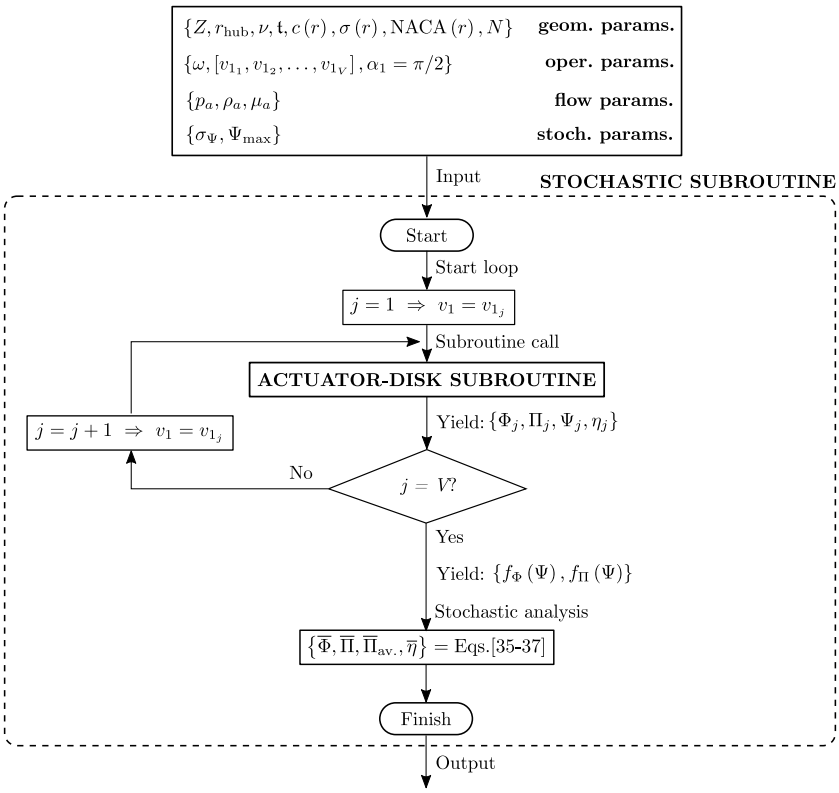

Fig. A.2. Flowchart of stochastic subroutine.

References

Abbasi, Reza, Ketabdari, Mohammad Javad, 2022. Enhancement of OWC Wells turbine efficiency and performance using riblets covered blades, a numerical study. Energy Convers. Manage. 254 (October 2021), 115212.

Addamo, Anna M., Calvo-Santos, Angel, Guillén, Jordi, Neehus, Sarah, Peralta-Baptista, Ana, Petrucco, Giacomo, Quatrini, Simone, Telsnig, Thomas, 2022. The EU Blue Economy Report 2022. Technical Report, European Comission, p. 232.

Alves, João S., Gato, Luís M.C., Falcão, António F.O., Henriques, João C.C., 2021. Experimental investigation on performance improvement by mid-plane guide-vanes in a biplane-rotor Wells turbine for wave energy conversion. Renew. Sustain. Energy Rev. 150 (October), 111497.

Arumugam, Pappu, Ramalingam, Velraj, Bhaganagar, Kiran, 2021. A pathway towards sustainable development of small capacity horizontal axis wind turbines – Identification of influencing design parameters & their role on performance analysis. Sustain. Energy Technol. Assess. 44.

Babintsev, Ivan Andreevich, 1975. Apparatus for converting sea wave energy into electrical energy. U.S. Patent No. 3922739.

Bassetti, M., Corsini, A., Delibra, G., Faggiolati, G., Piccinini, S., Rsipoli, F., Romani, G., Ruggieri, M., Tucimei, E., 2013. An integrated procedure for the design of a Wells turbine developed for Mediterranean operation. In: Proceedings of the European Seminar OWEMES 2012. ENEA, p. 560.

Biscay Marine Energy Platform (BIMEP) - Technical characteristics, 2022. URL https://www.bimep.com/en/bimep-area/technical-characteristics/.

Carrelhas, A.A.D., Gato, L.M.C., Henriques, J.C.C., Falcão, A.F.O., Varandas, J., 2019. Test results of a 30 kW self-rectifying biradial air turbine-generator prototype. Renew. Sustain. Energy Rev. 109, 187–198.

Ciappi, Lorenzo, 2020. Wave-to-Wire Modelling of Oscillating Water Column Wave Energy Converters and Deisgn Optimisation for the Mediterranean Sea (Ph.D. thesis). Università Degli Studi Firenze, p. 520.

Ciappi, Lorenzo, Cheli, Lapo, Simonetti, Irene, Bianchini, Alessandro, Manfrida, Giampaolo, Cappietti, Lorenzo, 2020. Wave-to-wire model of an oscillating-water-column wave energy converter and its application to mediterranean energy hot-spots. Energies 13 (21).

Ciappi, Lorenzo, Simonetti, Irene, Bianchini, Alessandro, Cappietti, Lorenzo, Manfrida, Giampaolo, 2022. Application of integrated wave-to-wire modelling for the preliminary design of oscillating water column systems for installations in moderate wave climates. Renew. Energy 194, 232–248.

Curran, R., Gato, L.M.C., 1997. The energy conversion performance of several types of Wells turbine designs. Proc. Inst. Mech. Eng. A 211 (2), 133–145.

Das, Tapas K., Kerikous, Emeel, Venkatesan, Nithya, Janiga, Gabor, Thevenin, Dominique, Samad, Abdus, 2022. Performance improvement of a Wells turbine through an automated optimization technique. Energy Convers. Manage.: X 16 (August).

Dhanasekaran, T.S., Govardhan, M., 2005. Computational analysis of performance and flow investigation on Wells turbine for wave energy conversion. Renew. Energy 30 (14), 2129–2147.

Drela, Mark, 1989. XFOIL: An Analysis and Design System for Low Reynolds Number Airfoils. Technical Report, pp. 1–12.

Falcão, A.F. de O., 2002. Control of an oscillating-water-column wave power plant for maximum energy production. Appl. Ocean Res. 24 (2), 73–82.

Falcão, António F.de O., 2010. Wave energy utilization: A review of the technologies. Renew. Sustain. Energy Rev. 14 (3), 899–918.

Falcão, António F.O., Henriques, João C.C., 2016. Oscillating-water-column wave energy converters and air turbines: A review. Renew. Energy 85, 1391–1424.

Falcão, António F.O., Henriques, João C.C., Gato, Luís M.C., 2018. Self-rectifying air turbines for wave energy conversion: A comparative analysis. Renew. Sustain. Energy Rev. 91 (April), 1231–1241.

Falcão, António F.O., Henriques, João C.C., Gato, Luís M.C., Gomes, Rui P.F., 2014. Air turbine choice and optimization for floating oscillating-water-column wave energy converter. Ocean Eng. 75, 148–156.

Falcão, A.F. de O., Rodrigues, R.J.A., 2002. Stochastic modelling of OWC wave power plant performance. Appl. Ocean Res. 24 (2), 59–71.

Fusco, Francesco, Nolan, Gary, Ringwood, John, 2010. Variability reduction through optimal combination of wind/wave resources: An Irish case study. Energy 35 (1), 314–325.

Gato, L.M.C., De, A.F., 1988. Aerodynamics of the Wells turbine. Int. J. Mech. Sci. 30 (6), 383–395.

Gato, L.M.C., De, A.F., 1989. Aerodynamics of the Wells turbine: control by swinging rotor-blades. Int. J. Mech. Sci. 31 (6), 425–434.

Gato, L.M.C., Falcão, A.F. De O., 1984. On the theory of the Wells turbine. J. Eng. Gas Turb. Power 106 (3), 628–633.

Gato, L.M.C., Henriques, J.C.C., 1996. Optimization of symmetrical profiles for the Wells turbine rotor blades. Am. Soc. Mech. Eng. Fluids Eng. Div. (Publ.) FED 238 (July), 623–630.

Gato, L.M.C., Henriques, J.C.C., Carrelhas, A.A.D., 2022. Sea trial results of the biradial and Wells turbines at mutriku wave power plant. Energy Convers. Manage. 268 (July), 115936.

Gato, L.M.C., Webster, M., 2001. An experimental investigation into the effect of rotor blade sweep on the performance of the variable-pitch Wells turbine. Proc. Inst. Mech. Eng. A 215 (5), 611–622.

Ghisu, Tiziano, Parks, Geoffrey T., Jarrett, Jerome P., Clarkson, P. John, 2011. Robust design optimization of gas turbine compression systems. J. Propuls. Power 27 (2), 282–295.

Gratton, Tim, Ghisu, Tiziano, Parks, Geoff, Cambuli, Francesco, Puddu, Pierpaolo, 2018. Optimization of blade profiles for the Wells turbine. Ocean Eng. 169 (August), 202–214.

Halder, Paresh, Mohamed, Mohamed H., Samad, Abdus, 2018. Wave energy conversion: design and shape optimization. Ocean Eng. 150 (December 2017), 337–351.

Halder, Paresh, Samad, Abdus, 2016. Torque and efficiency maximization for a wave energy harvesting turbine: an approach to modify multiple design variables. Int. J. Energy Res..

Hasselmann, Klaus, Barnett, Tim P., Bouws, E., Carlson, H., Cartwright, David E., Enke, K., Ewing, J.A., Gienapp, A., Hasselmann, D.E., Kruseman, P., et al., 1973. Measurements of wind-wave growth and swell decay during the joint north sea wave project (JONSWAP). In: Ergaenzungsheft zur Deutschen Hydrographischen Zeitschrift, Reihe A.

Hawthorne, W.R., Horlock, J.H., 1962. Actuator disc theory of the incompressible flow in axial compressors. Proc. Inst. Mech. Eng. 176 (1), 789–814.

Hu, Huakun, Xue, Wendong, Jiang, Peng, Li, Yong, 2022. Bibliometric analysis for ocean renewable energy: An comprehensive review for hotspots, frontiers, and emerging trends. Renew. Sustain. Energy Rev. 167 (June).

Ji, Yunguang, Yang, Zhikuo, Ran, Jingyu, Li, Hongtao, 2021. Multi-objective parameter optimization of turbine impeller based on RBF neural network and NSGA-II genetic algorithm. Energy Rep. 7, 584–593.

Kinoue, Y., Kim, T.H., Setoguchi, T., Kaneko, K., Takao, M., Lee, Y.W., 2002. Air Turbine Using Self-Pitch-Controlled Blades For Wave Energy Conversion. In: International Ocean and Polar Engineering Conference, All Days.

Kotb, Ahmed T.M., Nawar, Mohamed A.A., Attai, Youssef A., Mohamed, Mohamed H., 2022. Performance assessment of a modified Wells turbine using an integrated casing groove and Gurney flap design for wave energy conversion. Renew. Energy 197 (August), 627–642.

Kumar, P. Madhan, Halder, Paresh, Husain, Afzal, Samad, Abdus, 2019. Performance enhancement of Wells turbine: combined radiused edge blade tip, static extended trailing edge, and variable thickness modifications. Ocean Eng. 185 (May), 47–58.

Li, Ming, Luo, Haojie, Zhou, Shijie, Senthil Kumar, Gokula Manikandan, Guo, Xinman, Law, Tin Chung, Cao, Sunliang, 2022. State-of-the-art review of the flexibility and feasibility of emerging offshore and coastal ocean energy technologies in east and southeast Asia. Renew. Sustain. Energy Rev. 162 (August 2021).

Licheri, Fabio, Ghisu, Tiziano, Cambuli, Francesco, Puddu, Pierpaolo, 2022. Detailed investigation of the local flow-field in a Wells turbine coupled to an OWC simulator. Renew. Energy 197 (August), 583–593.

Mahrooghi, Ali, Lakzian, Esmail, 2021. Optimization of Wells turbine performance using a hybrid artificial neural fuzzy inference system (ANFIS) - genetic algorithm (GA). Ocean Eng. 226 (March).

Mohamed, M.H., Janiga, G., Pap, E., Thévenin, D., 2011. Multi-objective optimization of the airfoil shape of Wells turbine used for wave energy conversion. Energy 36 (1), 438–446.

Mohamed, M.H., Shaaban, S., 2013. Optimization of blade pitch angle of an axial turbine used for wave energy conversion. Energy 56, 229–239.

Pourrajabian, Abolfazl, Dehghan, Maziar, Rahgozar, Saeed, 2021. Genetic algorithms for the design and optimization of horizontal axis wind turbine (HAWT) blades: A continuous approach or a binary one? Sustain. Energy Technol. Assess. 44.

Raghunathan, S., 1995. A methodology for Wells turbine design for wave energy conversion. Proc. Inst. Mech. Eng. A 209 (3), 221–232.

Raghunathan, S., Tan, C.P., Wells, N.A.J., 1982. Theory and performance of a Wells turbine. J. Energy 6 (2 , Mar.-Apr. 1982), 156–160.

Scholz, N., 1977. Aerodynamics of Cascades. Technical Report, p. 620.

Setoguchi, T., Raghunathan, S., Takao, M., Kaneko, K., 1997. Air-turbine with self-pitch-controlled blades for wave energy conversion (estimation of performances in periodically oscillating flow). Int. J. Rotat. Mach. 3 (4), 233–238.

Setoguchi, Toshiaki, Takao, Manabu, 2006. Current status of self rectifying air turbines for wave energy conversion. Energy Convers. Manage. 47, 2382–2396.

Shaaban, Sameh, 2017. Wells turbine blade profile optimization for better wave energy capture. Int. J. Energy Res..

Shehata, Ahmed S., Xiao, Qing, Sqr, Khalid M., Day, Alexander, 2016. Wells turbine for wave energy conversion: a review. Int. J. Energy Res. 1–33.

Starzmann, R., Carolus, T.H., 2011. Effect of design parameters on aero-acoustic and aerodynamic performance of Wells turbines. In: Proceedings of the ASME 2011 30th International Conference on Ocean, Offshore and Arctic Engineering. Rotterdam, The Netherlands, pp. 1–10.

Starzmann, R., Carolus, T., 2013. Effect of blade skew strategies on the operating range and aeroacoustic performance of the Wells turbine. J. Turbomach. 136 (1).

Starzmann, Ralf, Carolus, Thomas, 2014. Model-based selection of full-scale Wells turbines for ocean wave energy conversion and prediction of their aerodynamic and acoustic performances. Proc. Inst. Mech. Eng. A 2–16.

Takao, Manabu, Setoguchi, Toshiaki, Kinoue, Yoichi, Kaneko, Kenji, 2007. Wells turbine with end plates for wave energy conversion. Ocean Eng. 34 (11), 1790–1795.

Torresi, M., Camporeale, S.M., Pascazio, G., 2009. Detailed CFD analysis of the steady flow in a Wells turbine under incipient and deep stall conditions. J. Fluids Eng. Trans. ASME 131 (7), 0711031–07110317.

Torresi, M., Camporeale, S.M., Strippoli, P.D., Pascazio, G., 2008. Accurate numerical simulation of a high solidity Wells turbine. Renew. Energy 33 (4), 735–747.

United Nations, 2022a. For a livable climate: Net-zero commitments. URL https://www.un.org/en/climatechange/net-zero-coalition.

United Nations, 2022b. The Paris agreements. URL https://www.un.org/en/climatechange/paris-agreement.

Weller, Sam, Parish, David N., Trnroos, Daniel, Johanning, Lars, 2017. Open sea OWC motions and mooring loads monitoring at BiMEP. In: Proceedings Of The 12th European Wave And Tidal Energy Conference, Vol. number August. Cork, Ireland, pp. 1–10.

Wells, A.A., 1976. Fluid driven rotary transducer. British Patent Spec. No. 1595700.

Yeo, Eng Jet, Kennedy, David M., O'Rourke, Fergal, 2022. Tidal current turbine blade optimisation with improved blade element momentum theory and a non-dominated sorting genetic algorithm. Energy 250.